

REPORT DOCUMENTATION PAGE				Form Approved OMB No. 0704-0188	
<p>Public reporting burden for this collection of information is estimated to average 1 hour per response, including the time for reviewing instructions, searching existing data sources, gathering and maintaining the data needed, and completing and reviewing the collection of information. Send comments regarding this burden estimate or any other aspect of this collection of information, including suggestions for reducing the burden, to Department of Defense, Washington Headquarters Services, Directorate for Information Operations and Reports (0704-0188), 1215 Jefferson Davis Highway, Suite 1204, Arlington, VA 22202-4302. Respondents should be aware that notwithstanding any other provision of law, no person shall be subject to any penalty for failing to comply with a collection of information if it does not display a currently valid OMB control number.</p> <p><b>PLEASE DO NOT RETURN YOUR FORM TO THE ABOVE ADDRESS.</b></p>					
<b>1. REPORT DATE (DD-MM-YYYY)</b> 07-01-2004		<b>2. REPORT TYPE</b> Final Report		<b>3. DATES COVERED (From - To)</b> 16 August 2002 - 16-Aug-03	
<b>4. TITLE AND SUBTITLE</b>  Grain-scale Crystal Plasticity Finite Element (FE) Simulations of Waspaloy During Hot Deformation			<b>5a. CONTRACT NUMBER</b> FA8655-02-M4060		
			<b>5b. GRANT NUMBER</b>		
			<b>5c. PROGRAM ELEMENT NUMBER</b>		
			<b>5d. PROJECT NUMBER</b>		
<b>6. AUTHOR(S)</b>  Professor Dierk R Raabe			<b>5d. TASK NUMBER</b>		
			<b>5e. WORK UNIT NUMBER</b>		
<b>7. PERFORMING ORGANIZATION NAME(S) AND ADDRESS(ES)</b> Max-Planck-Institut für Eisenforschung Max-Planck-Str. 1 Duesseldorf 40237 Germany			<b>8. PERFORMING ORGANIZATION REPORT NUMBER</b>  N/A		
<b>9. SPONSORING/MONITORING AGENCY NAME(S) AND ADDRESS(ES)</b>  EOARD PSC 802 BOX 14 FPO 09499-0014			<b>10. SPONSOR/MONITOR'S ACRONYM(S)</b>		
			<b>11. SPONSOR/MONITOR'S REPORT NUMBER(S)</b> SPC 02-4060		
<b>12. DISTRIBUTION/AVAILABILITY STATEMENT</b>  Approved for public release; distribution is unlimited.					
<b>13. SUPPLEMENTARY NOTES</b>					
<b>14. ABSTRACT</b>  This report results from a contract tasking Max-Planck-Institut für Eisenforschung as follows: The project aims to understand and predict the mechanical, crystallographic, and topological behavior of gamma grains in Waspaloy during plastic deformation at high temperature. The study will be conducted by use of a crystal plasticity finite element method that updates the local crystallographic and hardening state of the material via integration of the evolution equations for the crystal lattice orientation and the critical resolved shear stress.					
<b>15. SUBJECT TERMS</b> EOARD, Modeling & Simulation, Materials, Metals & alloys, Nickel, Superalloy					
<b>16. SECURITY CLASSIFICATION OF:</b>			<b>17. LIMITATION OF ABSTRACT</b> UL	<b>18. NUMBER OF PAGES</b> 40	<b>19a. NAME OF RESPONSIBLE PERSON</b> CHARLES H. WARD, Lt Col, USAF
<b>a. REPORT</b> UNCLAS	<b>b. ABSTRACT</b> UNCLAS	<b>c. THIS PAGE</b> UNCLAS			<b>19b. TELEPHONE NUMBER (Include area code)</b> +44 (0)20 7514 3154

20040225 096

**(1) In accordance with Defense Federal Acquisition Regulation 252.227-7036,  
Declaration of Technical Data Conformity (Jan 1997),**

"The Contractor, Max-Planck-Institut für Eisenforschung, hereby declares that, to the best of its knowledge and belief, the technical data delivered herewith under Contract No. FA8655-02-M4060 is complete, accurate, and complies with all requirements of the contract.

DATE:

Jan 11<sup>th</sup> 2004

Name and Title of Authorized Official:

RAABE, DIERK

**(2) In accordance with the requirements in Federal Acquisition Regulation  
52.227-13, Patent Rights—Acquisition by the U.S. Government (Jun 1989),  
PLEASE SELECT ONE OF THE FOLLOWING STATEMENTS & DELETE THE  
OTHER:**

(A) "Disclosures of all subject inventions as defined in FAR 52.227-13 have been reported in accordance with this clause."

Or,

(B) "I certify that there were no subject inventions to declare as defined in FAR 52.227-13, during the performance of this contract."

DATE:

Jan 11<sup>th</sup> 2004

Name and Title of Authorized Official:

RAABE, DIERK

## **Final Report (January, 7<sup>th</sup> 2004)**

(Block 17 of DD 1155, Accounting and Appropriation Data: F7LEOA22120600)

(AA 5723600 292 47DP 614113 6RER36 592 61102F 678900)

CONTRACT AGREEMENT NO. FA8655-02-M-4060

issued and administered by EUROPEAN OFFICE OF AEROSPACE, RESEARCH AND  
DEVELOPMENT, 223/231 OLD MARYLEBONE RD, LONDON NW1 5TH, BETH WANN 0207-514  
X4952, Beth.Wann@london.af.mil

# **Final Report on Grain-Scale Crystal Plasticity Finite Element Simulations of Waspaloy During Hot Deformation**

*Professor Dierk Raabe*

*Max-Planck-Institut für Eisenforschung  
Max-Planck-Str. 1  
40237 Düsseldorf  
Germany  
(raabe@mpie.de)*



# Contents

1.	Introduction.....	3
2.	Technical background and motivation .....	3
3.	Using texture components in crystal plasticity finite element simulations .....	4
3.1	Introduction to the method .....	4
3.2	Texture components .....	7
3.3	The crystal plasticity constitutive model.....	8
3.4	Using texture components in a crystal plasticity finite element simulation .....	10
4.	Description of the model set-up .....	12
5.	Determination of the constitutive material parameters for the compression simulations .....	12
6.	Results and discussion.....	14
6.1	Results for perfectly oriented cube crystals and different slip systems during compression deformation (<001> axis parallel to compression axis, no initial scatter) .....	14
6.2	Effect of orientational scatter prior to loading on in-grain texture evolution and grain fragmentation (<001> axis parallel to compression axis).....	16
6.3	Effect of orientational scatter prior to loading on the lateral misorientation arrangement and on the mechanical properties (<001> axis parallel to compression axis) using {111}<110> slip systems...	19
6.4	Effect of orientational scatter prior to loading on the lateral misorientation arrangement and on the mechanical properties (<001> axis parallel to compression axis) using {111}[110] and {110}[110]-type slip systems.....	23
6.5	Influence of friction on in-grain texture evolution and grain fragmentation for a cube-oriented grain	
	Introduction.....	26
	Orientalational stability of an ideal cube single crystal .....	27
	Orientalational stability of a cube single crystal with Gaussian orientation scatter.....	27
	Orientalational stability of a cube single crystal with Gaussian orientation scatter under large-friction conditions .	29
	Orientalational stability of a cube single crystal with Gaussian orientation scatter under surround friction conditions .....	30
	Influence of initial orientation scatter and of friction on the re-orientation behavior of cube crystals .....	31
	Conclusions for the friction study.....	32
6.6	Improved FE model set-up with finer mesh – simulation of Cube and 90° inclined Cube compression.....	33
	Mesh design and FE set-up .....	33
	Constitutive data fit.....	34
	Texture analysis after compression of a Cube orientation and a Goss orientation.....	35
7.	Conclusions.....	38



## 1. Introduction

This report presents the results obtained from crystal plasticity FEM simulations of Waspaloy compression deformation experiments. The work was conducted under the framework of a mini-program on "Grain-scale Crystal Plasticity Finite Element Simulations of Waspaloy During Hot Deformation". The project was issued and administered by the EUROPEAN OFFICE OF AEROSPACE, RESEARCH AND DEVELOPMENT under the accounting and appropriation data F7LEOA22120600 (AA 5723600 292 47DP 614113 6RER36 592 61102F 678900) and contract agreement number FA8655-02-M-4060.

## 2. Technical background and motivation

The development of polycrystalline, directionally solidified, and even single crystal superalloys and their introduction into commercial application as turbine blades is one of the major technological achievements in materials science over the past decades [1-2]. The mini-program on "Grain-scale Crystal Plasticity Finite Element Simulations of Waspaloy During Hot Deformation" is a numerical study which aims at understanding and predicting the nonuniformity of texture and strain during hot compression of columnar grain structures having **different orientations** relative to the forging direction. The modeling of deformation-induced plastic instabilities is of substantial relevance for understanding the recrystallization of Waspalloy during or after hot compression. Such knowledge is important for obtaining homogeneously recrystallized material after forging of cast blocks which have a coarse initial grain structure. A refined homogeneous microstructure leads to much better mechanical properties when compared to coarse grained material. The current crystal plasticity FEM simulation study is in particular conducted for learning more about the origin of nucleation sites for dynamic recrystallization inside deformed grains.

The **first part of the study**, which was delivered in April 2003 was in the form of an intermediate report which contained three main work packages. These were first, the formulation of a conceptually flexible and microstructurally adequate crystal-based FEM model, which allows one to study crystallographic effects on the formation of in-grain orientational gradients in Waspaloy during plastic compression. The model approach which turned out to be most suited for this task is the texture component crystal plasticity finite element method [12]. Second, I had to make considerations about the potential slip systems. Although 12 slip systems of type  $\{111\}\langle 110 \rangle$  are commonly used in crystal plasticity simulations for FCC and crystallographically related materials recent single crystal experiments have shown that



Waspaloy and other FCC materials also tend, at elevated temperatures, to deform additionally on non-octahedral  $\{110\}\langle 1\bar{1}0\rangle$  slip systems. Third, the constitutive behavior had to be derived by fitting the plastic behavior of Waspaloy to mechanical data measured by Dr. Semiatin.

The consideration of **non-octahedral** together with octahedral slip systems into the simulations and fitting procedures requires some comments because one has commonly used only 12 slip systems,  $\{111\}\langle 1\bar{1}0\rangle$ , in corresponding crystal plasticity simulations of the deformation of fcc single crystals. However, experiments have shown that single crystal Waspaloy also tends, at elevated temperatures, to deform also on  $\{110\}\langle 1\bar{1}0\rangle$  slip systems. Therefore, in the present crystal plasticity simulations of high-temperature deformation of cube oriented and related coarse grained Waspaloy microstructures octahedral and non-octahedral slip systems are considered. This approach of considering also non-octahedral slip systems is based on experimental studies and numerical models of the high-temperature deformation behavior of single crystalline superalloys [1-4]. For nickel-base superalloys in general, and FCC single crystal materials in particular, experiments show different operating slip systems such as  $\{111\}\langle 110\rangle$ ,  $\{111\}\langle 112\rangle$ , and  $\{110\}\langle 110\rangle$  [1-2]. Knowles et al. [1] considered  $\{111\}\langle 112\rangle$  slip systems for a study on creep of single crystal superalloy CMSX-4. Ghosh et al. [2] considered  $\{001\}\langle 110\rangle$  slip systems for modeling crystallographic anisotropy.

### 3. Using texture components in crystal plasticity finite element simulations

#### 3.1 Introduction to the method

Metals mostly occur in polycrystalline form where each grain has a different crystallographic orientation, shape, and volume fraction. The distribution of the grain orientations is referred to as crystallographic texture. The discrete nature of crystallographic slip along certain lattice directions on preferred crystallographic planes entails an anisotropic plastic response of such samples under mechanical loads. While the elastic-plastic deformation of single crystals and bicrystals can nowadays be well predicted, plasticity of polycrystalline matter is less well understood. This is essentially due to the intricate interaction of the grains during co-deformation. This interaction leads to strong in-grain and grain-to-grain heterogeneity in terms of strain, stress, and crystal orientation. One major aim of polycrystal research consequently lies in identifying adequate measures for mapping initial crystallographic anisotropy into mathematical methods for predicting large strain plastic deformation of polycrystalline matter. The second even more demanding goal is the prediction of the **evolution of crystalline anisotropy** during plastic deformation. This is necessary since the crystals individually rotate during deformation owing to the nonsymmetry of the displacement gradients created by crystal slip. The complex microstructural processes involved during these reorientation processes of the individual grain



portions in polycrystalline matter cannot be captured in terms of simple empirical constitutive laws but require the use of physically-based concepts. In this context the crystal plasticity finite element constitutive methods have increasingly gained momentum. In these approaches one typically assumes the stress response at each macroscopic continuum material point to be potentially given by one crystal or by a volume-averaged response of a set of grains comprising the respective material point. The latter method naturally involves local homogenization. Compared to isotropic J2 approaches the crystal plasticity finite element method reduces the degrees of freedom for the displacement field at each integration point to the crystallographic slip dyads transformed according to the local grain orientation. Representing and updating the crystallographic orientation at each Gauss point renders crystallographically discrete plasticity simulations powerful tools for investigating anisotropy and the evolution of deformation textures. This chapter addresses the question how crystallographic textures can be merged with crystal plasticity finite element constitutive descriptions in a more rigorous, scalable, and efficient way. A special challenge in this context lies in the reduction of redundant texture information to a level where sufficient details can be recovered without losing physical significance.

This rather complex problem of representing large microtexture sets in plasticity simulations can be split into two separate tasks. The first one is the formulation of a solution method which uses the crystallographic orientation as a state variable. This is typically achieved by formulating an orientation dependent constitutive law which maps the requested physical anisotropy at the single crystal scale and by embedding this formulation into a finite element code. The numerical implementation then tackles the interaction of the differently oriented volume portions and thereby predicts the integral response of the sample under loads. Any such formulation requires a *discrete* representation of the orientation distribution function or a portion of it at each integration point. Therefore, the second task consists in feeding one *single* rotation matrix (crystal orientation) directly on each Gauss point of the finite element mesh. This amounts to mapping or respectively decomposing orientation distributions in such a way that they can be subsequently mapped on a mesh in a discrete manner thereby matching the initial overall distribution.

One method to map large texture data sets onto a discrete mesh could be to simply assign each prescribed or measured discrete orientation matrix to an individual grid point using. This is indeed the classical approach which is currently used by many crystal plasticity finite element modelers. However, such an orientation-by-orientation (or grain-by-grain) approach is not practicable when conducting forming simulations of larger parts typically containing more than  $10^{10}$  separate crystals. The second idea, therefore, is to formulate a *scalable* method for including textures in crystal plasticity finite element simulations. Scalability means in this context to feed large as well as small texture data sets into finite element models, but with exact quantification of the crystallographic error arising from such data reduction.

Before discussing the advantages and disadvantages of the various functions available for the



reproduction of textures it must be noted that crystal plasticity finite element approaches require a *discrete* representation of the orientation distribution function or a portion of it at each integration point. Mapping a discrete part of a global texture to a Gauss point or to a set of Gauss points requires a method which is physically meaningful (avoiding over-simplification) and which at the same time reduces the texture information content to a level which is necessary to treat complex forming situations at reasonable computation costs (avoiding over-modeling). Such a form is offered in particular by the texture component method. It approximates the orientation distribution function by a superposition of sets of simple standard functions with individual spherical coordinates, orientation density, and scatter in orientation space. Such a representation of a preferred orientation is referred to as a texture component. In contrast to the use of global symmetric Wigner functions for instance in the Fourier-type series expansion methods, the texture component method is based on using localized spherical normalized standard functions.

A new concept for representing textures efficiently in plasticity simulations is based on mapping small sets of mathematically compact **spherical Gaussian texture components** on the integration points of a **crystal plasticity finite element model**. This is done in two steps: First, by extracting the texture components and the random background from experimental starting textures. Second, by decomposing these functions into sets of discrete orientations which altogether exactly represent the original Gauss shape of each component (in orientation space) so that they can be mapped as lateral distributions onto a discrete lattice. The initial spherical distribution is thereby transformed into a spherical *and* lateral distribution. During the subsequent crystal plasticity finite element simulation the texture component method loses its significance since each individual orientation originally pertaining to one of the texture components can undergo *individual* re-orientation as in any of the above quoted crystal plasticity methods. In order to avoid confusion one should, therefore, underline that the texture component method is used to *feed* textures into finite element simulations on a strict physical and quantitative basis. The components as such, however, are not further tracked as functions during the simulation. On the other hand the mapped orientation points which were extracted from the components must not be confused with individual grains, but they are points of a distribution function.

The **texture component approach** ensures that the mapping of textures can be linked to materials concepts since texture components can be directly interpreted in terms of characteristic metallurgical mechanisms. Furthermore it makes sure that redundant texture information which is less relevant, for instance to predict plastic anisotropy, can be reduced in the input data set. The following chapters explain the method in more detail and give examples. An overview of the new method is given in [12].





### 3.2 Texture components

The texture component method offers a useful approach in the context described above. It is a technique of approximating the orientation distribution function in the form of discrete sets of symmetrical spherical model functions which are defined in orientation space. The model functions have individual height and individual full width at half maximum as a measure for the strength and scatter of the crystallographic texture component they represent. They are typically formulated as central functions which have an isotropic scatter in orientation space. The mathematical reproduction of the orientation distribution function by texture component functions can be expressed by the superposition

$$f(g) = F + \sum_{c=1}^C I^c f^c(g) = \sum_{c=0}^C I^c f^c(g) \quad \text{where} \quad I^0 = F, f^0(g) = 1 \quad (1)$$

where  $g$  is the orientation,  $f(g)$  is the orientation distribution function, and  $F$  is the volume portion of all randomly oriented crystals (random texture component).  $F$  may be understood as the intensity of the only *global* component used in the approximation, equivalent to  $f^c(g) = 1$  for each orientation point in Euler space,  $g \in G$ . The intensity  $I^c$  describes the volume fraction of all crystallites belonging to the component  $c$ . The orientation density of the component is described by a central function, i.e. its value decreases isotropically with increasing orientation distance  $\tilde{\omega}^c = \tilde{\omega}(g^c, g)$  from the maximum. This means that  $f^c(g)$  only depends on  $\tilde{\omega}^c = \tilde{\omega}(g^c, g)$ , but it is independent on the rotation axis  $\tilde{n}^c$ .

The orientation distribution function is defined by

$$f(g) dg = 8 \pi^2 \frac{dV_g}{V} \quad \text{which implies} \quad f(g) \geq 0 \quad (2)$$

where  $V$  is the sample volume and  $dV_g$  the volume of all crystals with an orientation  $g$  within the orientation portion  $dg = \sin(\phi) d\phi d\varphi_1 d\varphi_2$ . Normalization requires

$$\oint f^c(g) dg = 1 \quad \text{which implies} \quad \sum_{c=0}^C I^c = 1 \quad (3)$$

As a rule texture components require positivity, i.e.

$$f^c(g) \geq 0 \quad \text{for all} \quad g \in G \quad \text{and} \quad I^c > 0 \quad (4)$$

where  $G$  is the orientation space.

Spherical central functions, including corresponding pole figures, can generally be represented in the form of series expansions of  $\chi$  functions or respectively Legendre polynomials. More practical approximations of texture components have been introduced on the basis of spherical Gauss- and Lorentz-functions. The work presented in this study makes use of Gauss-shaped model functions for the decomposition of the orientation distribution function which are described by



$$f^c(g) = N^c \exp(S^c \cos \tilde{\omega}) \quad (5)$$

where

$$S^c = \frac{\ln 2}{1 - \cos(b^c/2)} \quad \text{and} \quad N^c = \frac{1}{I_0(S^c) - I_1(S^c)} \quad (6)$$

The according pole figure projections  $P_h^M(g^c, b^c, y)$  can be calculated in closed analytical form

$$P_h^M(g^c, b^c, y) = N^c \exp(S^c \sin(\nu^c/2)) I_0(S^c \cos(\nu^c/2)) \quad (7)$$

where  $\nu^c$  describes the geometry of the component in the respective pole figure projection and  $I_l(x)$  are generalized Bessel functions. The value  $b^c$  is the halfwidth and can be interpreted as the mean diameter of a spherical component in orientation space and  $g^c$  is the center orientation of the texture component.

The components describing  $f(g)$  can be determined by the best fit of the experimental pole figure input data  $\tilde{P}_{h_i}^M(y_r)/N_{h_i}$  with the recalculated pole figures  $\sum_c I^c \tilde{P}_{h_i}^M(g^c, b^c, y_r)$ . The index  $r$  marks the measured sample directions  $y_r$ . The component parameters  $I^c$ ,  $g^c$  and  $b^c$  and the normalization  $N_{h_i}$  of the pole figures are obtained by solving the least squares problem

$$\sum_{i,r} w_{ir} \left[ \tilde{P}_{h_i}(y_r)/N_{h_i} - \sum_c I^c \tilde{P}_{h_i}^M(g^c, b^c, y_r) \right]^2 \Rightarrow \text{Min.} \quad (8)$$

where  $w_{ir}$  are weight factors. Usually the parameters  $g^c$  and  $b^c$  must be calculated by a non-linear algorithm. First estimates are required, which may be obtained manually from the graphical representation of the difference pole figures which are calculated according to

$$\Delta_{h_i}(y_r) = \tilde{P}_{h_i}(y_r) - \sum_c I^c \tilde{P}_{h_i}^M(g^c, b^c, y_r) \quad (9)$$

Depending on experience in interpreting crystallographic textures the user can specify the position, height, and scatter of the texture components within certain bounds before the minimization. This makes particularly good sense when the number of texture components initially prescribed to match an experimental texture is small or when a certain scatter width of the components should not be exceeded.

### 3.3 The crystal plasticity constitutive model

In this approach I use the large-strain constitutive crystal plasticity model originally suggested by Kalidindi [5-8]. In this formulation one assumes the stress response at each macroscopic continuum material point to be potentially given by one crystal or by a volume-averaged response of a set of grains comprising the respective material point. The latter assumption can be



referred to as a local Taylor-type or local strain-rate homogenization assumption. In case of a multi-grain description the volume averaged stress amounts to

$$\langle \mathbf{T} \rangle = \sum_{k=1}^N (w_k \mathbf{T}_k) \quad (10)$$

where  $N$  is the total number of individual orientations mapped onto an integration point using the Taylor assumption,  $w_k$  the volume fraction of each single orientation extracted from a texture component as described above,  $\mathbf{T}_k$  the Cauchy stress produced by the  $k$ th individual orientation, and  $\langle \mathbf{T} \rangle$  the volume average stress produced by all orientation mapped at the integration point. The constitutive equation for the stress in each grain is then expressed in terms of

$$\mathbf{T}^* = \mathbf{C} \mathbf{E}^* \quad (11)$$

where  $\mathbf{C}$  is the fourth order elastic tensor and  $\mathbf{E}^*$  an elastic strain measure,

$$\mathbf{E}^* = \frac{1}{2} (\mathbf{F}^{*T} \mathbf{F}^* - \mathbf{1}) \quad (12)$$

obtained by the polar decomposition,

$$\mathbf{F} = \mathbf{F}^* \mathbf{F}^p \quad (13)$$

which leads to a stress measure which is the elastic work conjugate to the strain measure  $\mathbf{E}^*$ ,

$$\mathbf{T}^* = \mathbf{F}^{*-1} (\det(\mathbf{F}^*) \mathbf{T}) (\mathbf{F}^*)^{-T} \quad (14)$$

where  $\mathbf{T}$  is the symmetric Cauchy stress tensor in the grain, and  $\mathbf{F}^*$  is a local elastic deformation gradient defined in terms of the local *total* deformation gradient  $\mathbf{F}$  and the local *plastic* deformation gradient  $\mathbf{F}^p$ . According to equation (12) the relation between the elastic and the plastic portion of  $\mathbf{F}$  amounts to

$$\mathbf{F}^* = \mathbf{F} (\mathbf{F}^p)^{-1}, \quad \det(\mathbf{F}^*) > 0, \quad \det(\mathbf{F}^p) = 1 \quad (15)$$

The plastic deformation gradient is given by the flow rule

$$\dot{\mathbf{F}}^p = \mathbf{L}^p \mathbf{F}^p \quad (16)$$

with its crystalline portion

$$\mathbf{L}^p = \sum_{k=1}^N \dot{\gamma}_k \mathbf{m}_k, \quad \mathbf{m}_k = \hat{\mathbf{b}}_k \otimes \hat{\mathbf{n}}_k \quad (17)$$

where  $\mathbf{m}_k$  are the  $k$ th dyadic slip products of unit vectors  $\hat{\mathbf{b}}_k$  in the slip direction and  $\hat{\mathbf{n}}_k$  normal to the slip plane, and  $\dot{\gamma}_k$  the shear rates on these systems. The specific constitutive functions for the plastic shearing rates  $\dot{\gamma}_k$  on the slip systems are taken as

$$\dot{\gamma}_k = \dot{\gamma}_o \left| \frac{\tau_k}{\tau_{k,crit}} \right|^{\frac{1}{m}} \text{sgn}(\tau_k) \quad (18)$$

where  $\tau_k$  is the resolved shear stress for the slip system  $k$ , and  $\tau_{k,crit}$  is the actual critical shear stress on the  $k$ th slip system.  $\dot{\gamma}_o$  and  $m$  are material parameters representing shearing rate and the



rate sensitivity of slip. The calculation of  $\tau_{k,\text{crit}}$  has been achieved by accounting for latent hardening through the use of an appropriate hardening matrix,

$$\dot{\tau}_{k,\text{crit}} = \sum_i h^{ki} |\dot{\gamma}^i|, \quad h^{ki} = q^{ki} h^{(i)} \quad (19)$$

where  $h^{ki}$  is the rate of strain hardening on  $k$ th slip system due to a shearing on  $i$ th slip system,  $q^{ki}$  is the hardening matrix describing the latent hardening behavior of a crystallite, and  $h^{(i)}$  is the hardening rate of the single slip system  $i$ .

### 3.4 Using texture components in a crystal plasticity finite element simulation

The main task of the new concept is to represent sets of spherical Gaussian **texture components** on the **integration points** of a **finite element mesh** for a crystal plasticity simulation. This procedure works in two steps: First, the discrete preferred orientation  $g^c$  (center orientation, mean orientation) is extracted from each of the texture components and assigned in terms of its respective Euler triple  $(\varphi_1, \phi, \varphi_2)$ , i.e. in the form of a *single* rotation matrix, onto *each* integration point (Fig. 1a). In the second step, these discrete orientations are re-oriented in such a fashion that their resulting overall distribution reproduces the texture function which was originally prescribed in the form of a Gaussian texture component. In other words the orientation scatter described initially by a texture component function is in the finite element mesh represented by a systematically re-oriented set of orientations, each assigned to one integration point, which reproduces the original spherical scatter prescribed by that component. This means that the scatter which was originally only given in orientation space is now represented by a distribution both, in real space and in orientation space, i.e. the initial spherical distribution is transformed into a spherical *and* lateral distribution. The described allocation and re-orientation procedure is formulated as a weighted sampling Monte Carlo integration scheme in Euler space. It is important in this context, that the use of the Taylor assumption locally allows one to map more than one preferred crystallographic orientation on each integration point and to assign to each of them an individual volume fraction. This means that the procedure of mapping and rotating single orientations in accord with the initial texture component scatter width is individually conducted for *all* prescribed components as well as for the random background extracted from initial experimental or theoretical data.



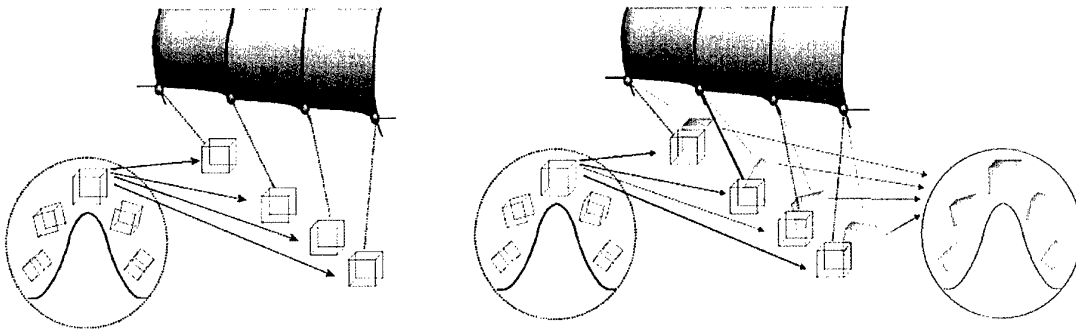


Figure 1 The decomposition of a cube-oriented spherical component consists in extracting the preferred orientation from the function (i.e.  $\varphi_1=0^\circ$ ,  $\phi=0^\circ$ ,  $\varphi_2=0^\circ$  for cube, Bunge-Euler notation) and assigning it in the form of a single rotation matrix onto each integration point (left hand side). In the second step (right hand side) all orientation portions, defined by the integration points, are re-oriented to reproduce the prescribed orientation distribution.

After decomposing and representing the initial texture components as a lateral and spherical single orientation distribution in the mesh, the texture component concept is no longer required in the further procedure. This is due to the fact that during the subsequent crystal plasticity finite element simulation each individual orientation originally pertaining to one of the texture components can undergo an *individual* orientation change as in the conventional crystal plasticity methods. This means that the texture component method loses its significance during the simulation. In order to avoid confusion one should, therefore, underline that the texture component method is used to *feed* textures of sets of sub-grains or grains into finite element simulations on a strict physical and quantitative basis. The components as such, however, are in their original form as compact functions not tracked during the simulation. It must also be noted that the orientation points which were originally obtained from the components do not represent individual *grains* but portions of an orientation distribution function. Details of this recently introduced texture component crystal plasticity finite element method are given in [9-14].

The constitutive model described above and the associated implicit time-integration procedure were implemented into the commercial finite element code MARC by means of the user defined material subroutine HYPELA2 [15].



#### 4. Description of the model set-up

The meshed sample was a cylinder with 10 mm in diameter and 15 mm in height. **Different initial crystallographic orientations** parallel to the loading axis were used for the simulations. Also, Compression was conducted at a simulated temperature of 1450 K (1177 °C), The strain rate was  $0.005 \text{ s}^{-1}$ . The reduction in height amounted to 50 % corresponding to a true strain of about 0.69. The friction in the two contact planes were assumed at first to be zero. A later part of the study investigates the influence of changes in the friction coefficients. A set of 40 eight-node 3D brick elements was used to discretize the mesh for the sample. The three-dimensional finite element mesh is shown in Fig. 2. The compression tool was modeled as a rigid surface.

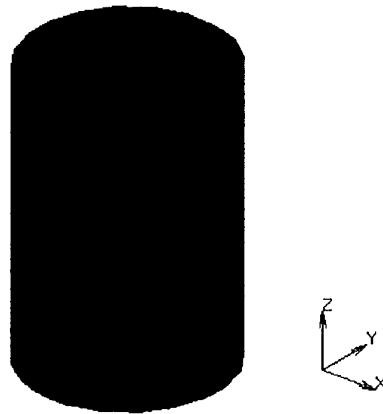


Fig. 2. The mesh used for the finite element discretization of the Waspaloy sample. Compression is conducted along the z-axis.

#### 5. Determination of the constitutive material parameters for the compression simulations

The values of the elastic parameters were taken to be those of pure single-crystalline nickel at room temperature, i.e.  $C_{11}=248.1 \text{ GPa}$ ,  $C_{12}=154.9 \text{ GPa}$ , and  $C_{44}=124.4 \text{ GPa}$  [16].

There are two flow parameters in the crystal plasticity constitutive equations, one is the reference value of slip rate, which is taken to be  $0.005 \text{ s}^{-1}$ , the other is slip-rate sensitivity parameter  $m$ , which is determined by the macroscopic strain-rate jump experiment in simple compression. According to the experimental data a value of  $m=0.2$  was used for the simulations.



The slip system hardening parameters were approximated by use of an iterative fashion by adjusting the values of these parameters in the finite element simulation of simple compression in such a way that the resulting stress-strain curve was in good correspondence with the experimental data. For 12 slip systems  $\{111\}\langle 1\bar{1}0\rangle$ , the estimated initial value of slip resistance  $s_0$  is 23.8798 MPa and the hardening parameter  $h_0$  is 0 MPa. For 18 slip systems including 12  $\{111\}\langle 1\bar{1}0\rangle$  and 6  $\{110\}\langle 1\bar{1}0\rangle$  the estimated initial value of slip resistance  $s_0$  is 25.6698 MPa and the hardening parameter  $h_0$  is 0 MPa. Fig. 3 shows the experimental data for the stress-strain response and the FEM model fit for that data.

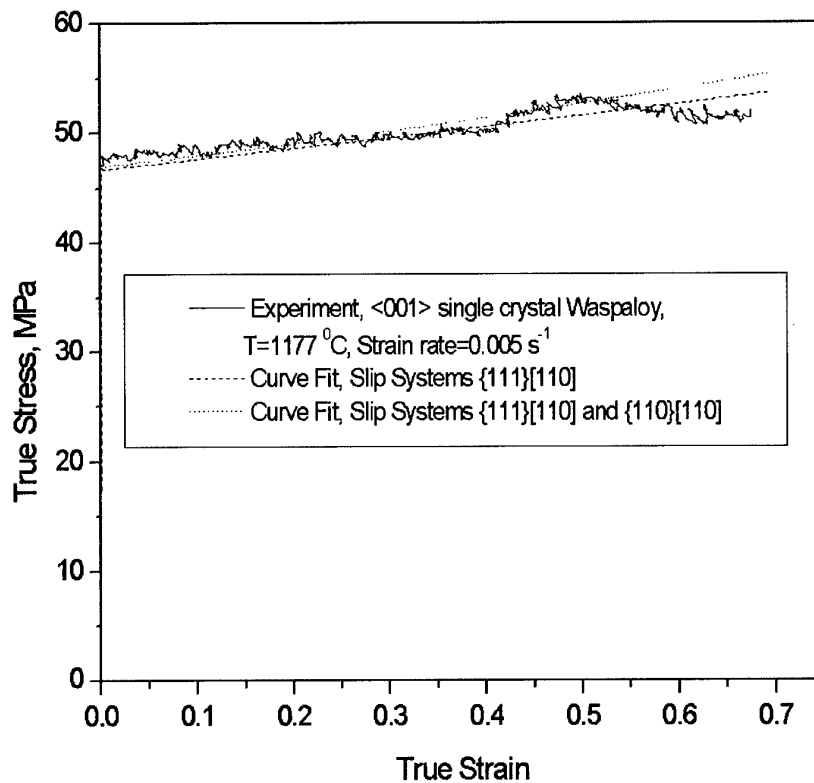


Fig. 3. Experimental data for the stress-strain response and the FEM model's fits for that data.



## 6. Results and discussion

### 6.1 Results for perfectly oriented cube crystals and different slip systems during compression deformation ( $\langle 001 \rangle$ axis parallel to compression axis, no initial scatter)

Figs. 4 and 5 show the pole figures and misorientation contour plots for the cube oriented single-crystal Waspaloy samples after deformation. The samples had no initial in-grain misorientation fluctuation, i.e. they were perfectly  $\langle 001 \rangle$  oriented parallel to the compression direction before the compression deformation. Fig. 4a shows the pole figure results obtained for a crystal plasticity simulation with  $\{111\}\langle 110 \rangle$  slip systems (assumption of low temperature deformation). Fig. 4b shows the pole figures obtained for a simulation with  $\{111\}\langle 110 \rangle$  and  $\{110\}\langle 110 \rangle$  slip systems (assumption of high temperature deformation). The simulations shown in Figs. 4 and 5 were conducted for initially perfect cube-oriented single-crystalline Waspaloy. This means that the texture component finite element simulations were conducted under the assumption of an orientational scatter of  $0^\circ$  about the exact cube orientation prior to loading. Figs. 4 and 5 show that there is a little lattice rotation for the  $\{111\}\langle 110 \rangle$  slip systems after compressing deformation, the maximum misorientation is  $1.428^\circ$ ; but for  $\{111\}\langle 110 \rangle$  and  $\{110\}\langle 110 \rangle$  slip systems, there is a large lattice rotation after compressing deformation.

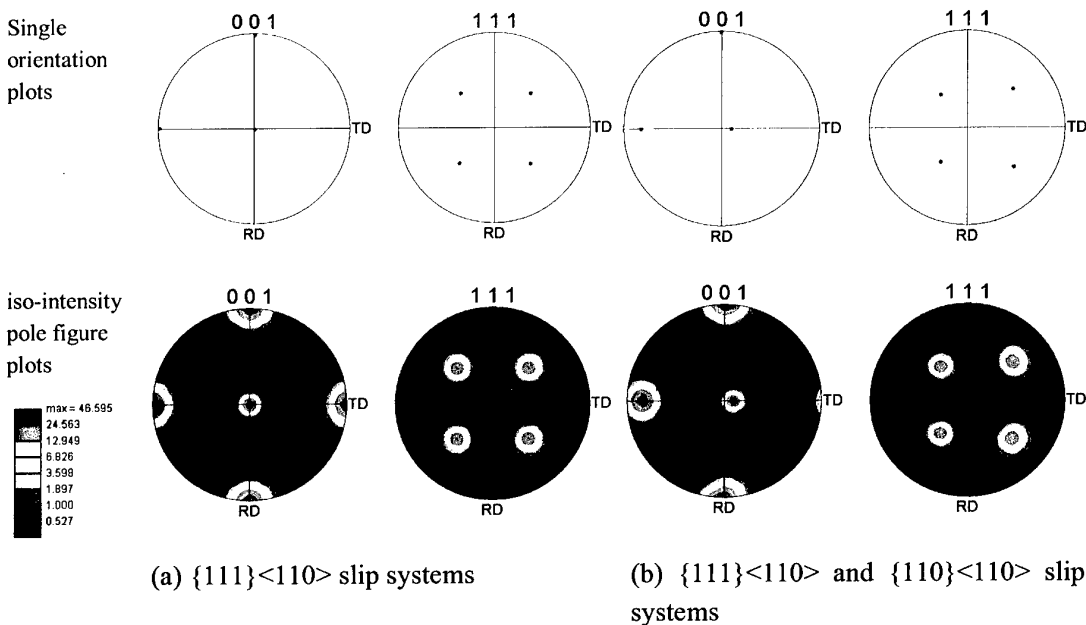
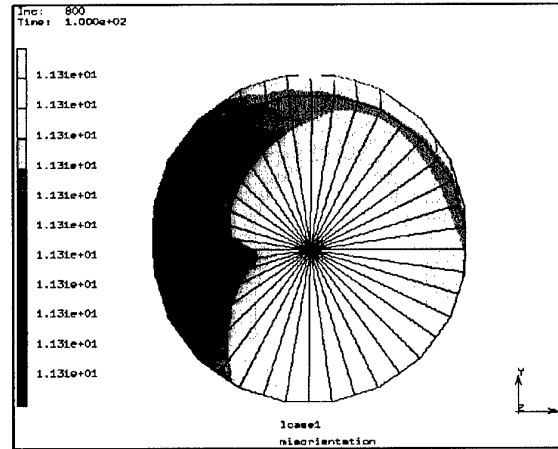
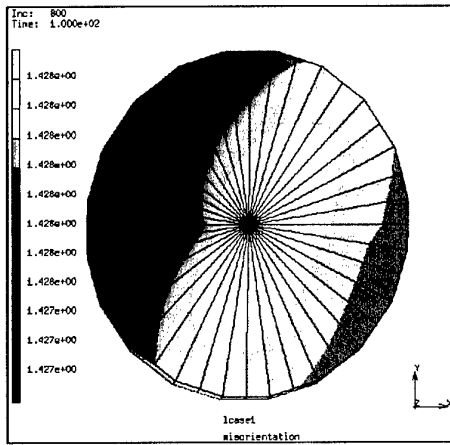


Fig. 4. Effect of slip system selection on pole figures for the cube orientation single-crystal Waspaloy, (a)  $\{111\}\langle 110 \rangle$  slip systems, (b)  $\{111\}\langle 110 \rangle$  and  $\{110\}\langle 110 \rangle$  slip systems. RD and TD are given as an arbitrary in-plane reference coordinate system. Compression (50% engineering thickness reduction) was conducted along the normal direction ND.





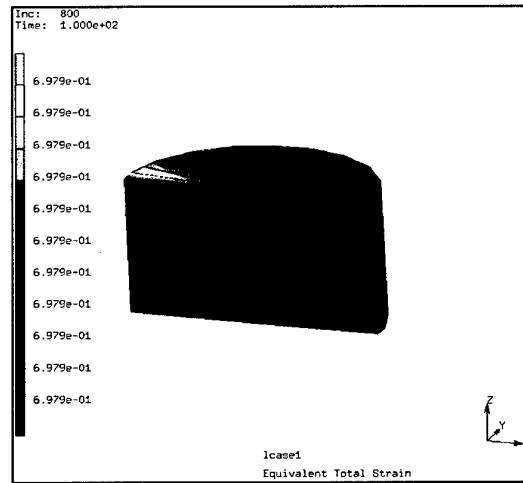
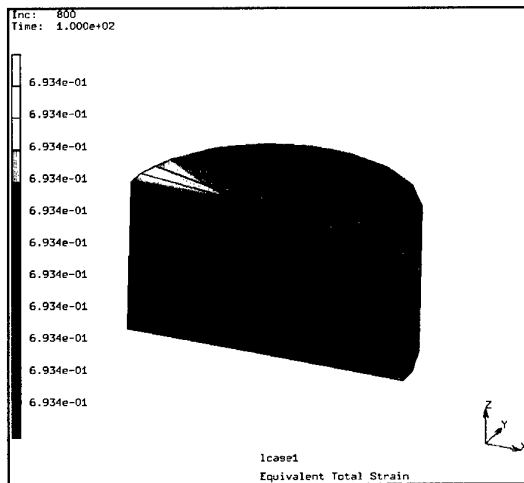


(a)  $\{111\}\langle 110 \rangle$  slip systems

(b)  $\{111\}\langle 110 \rangle$  and  $\{110\}\langle 110 \rangle$  slip systems

Fig. 5. Misorientation contours with (a)  $\{111\}\langle 110 \rangle$  slip systems and  $\{111\}\langle 110 \rangle$  and  $\{110\}\langle 110 \rangle$  slip systems, initial Cube orientation.

Fig. 6 shows the contour plots of the equivalent total strains and equivalent Von Mises stresses for the simulations obtained for the two different sets of potentially active slip systems. Fig. 6a shows the results obtained for  $\{111\}\langle 110 \rangle$  slip and Fig. 6b shows the data for  $\{111\}\langle 110 \rangle$  and  $\{110\}\langle 110 \rangle$  slip systems, respectively. The data show that the distribution of the equivalent total strain is similar for both cases. The equivalent Von Mises stresses are slightly different between the two cases.



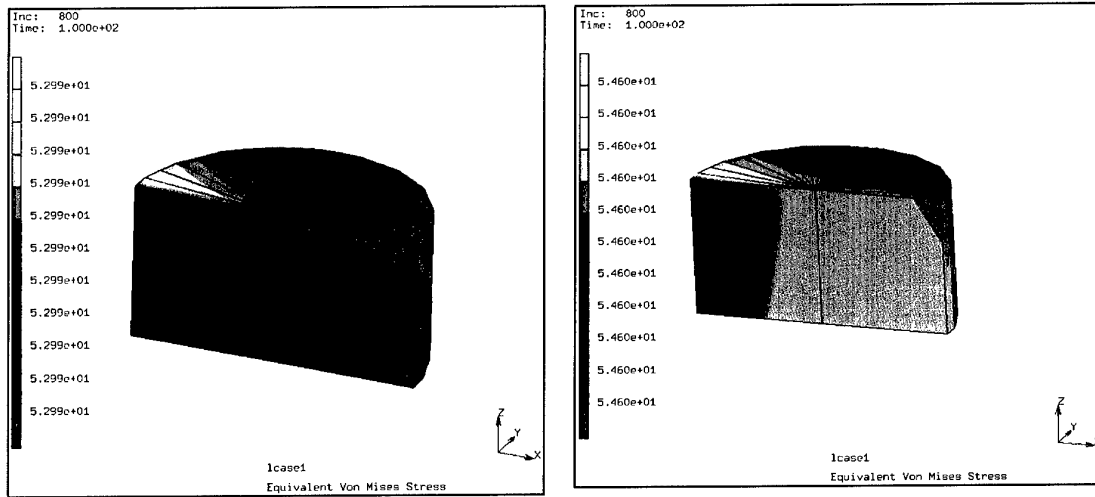
Equivalent total strain

(a)  $\{111\}\langle 110 \rangle$  slip systems

Equivalent total strain

(b)  $\{111\}\langle 110 \rangle$  and  $\{110\}\langle 110 \rangle$  slip systems





equivalent Von Mises Stress

(a)  $\{111\}\langle 110 \rangle$  slip systems

equivalent Von Mises Stress

(b)  $\{111\}\langle 110 \rangle$  and  $\{110\}\langle 110 \rangle$  slip systems

Fig. 6. The contours of equivalent total strains and equivalent Von Mises stresses with (a)  $\{111\}\langle 110 \rangle$  slip systems and (b)  $\{111\}\langle 110 \rangle$  and  $\{110\}\langle 110 \rangle$  slip systems.

## 6.2 Effect of orientational scatter prior to loading on in-grain texture evolution and grain fragmentation ( $\langle 001 \rangle$ axis parallel to compression axis)

Figs. 7 and 8 show the effects of the initial orientational scatter width on the in-grain texture evolution for close-to-cube oriented grains in terms of pole figures of the deformed (compressed) samples. The simulations were conducted for two sets of potentially active slip systems, namely, for  $\{111\}\langle 110 \rangle$  slip systems (Figs. 7a, 8a) and for  $\{111\}\langle 110 \rangle$  and  $\{110\}\langle 110 \rangle$  slip systems (Figs. 7b, 8b). The pole figures show the texture evolution after 50% compressing deformation for the two cases.



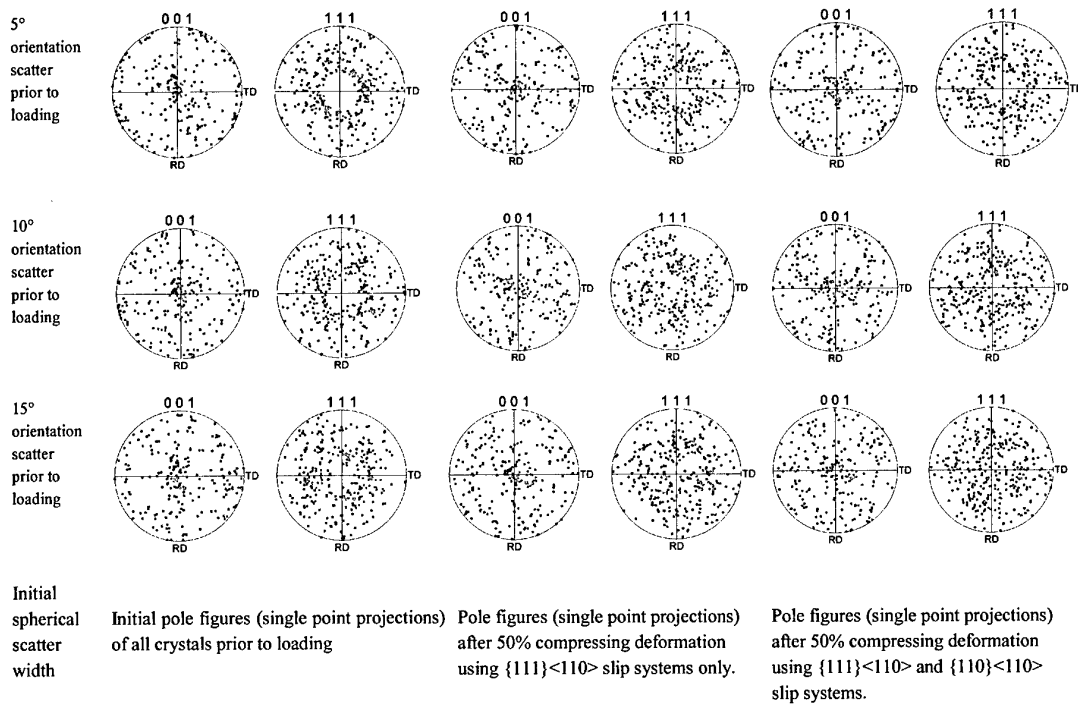
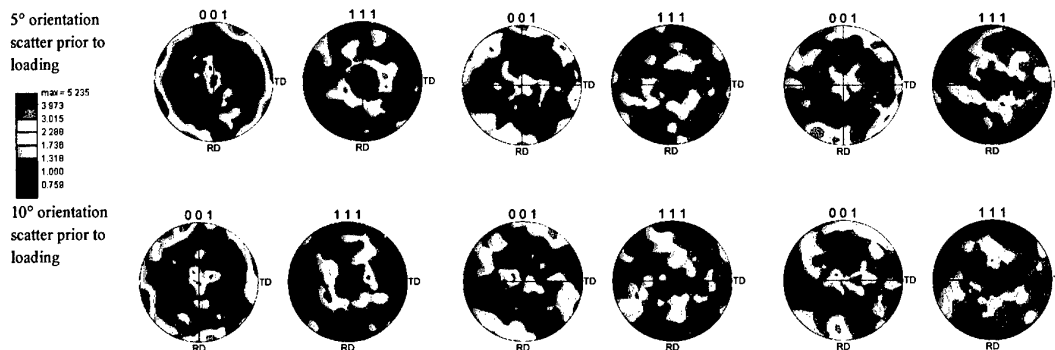


Fig. 7. Effect of the initial orientational scatter width on the in-grain texture evolution presented in terms of pole figures after deformation with  $\{111\}\langle 110 \rangle$  slip systems (a);  $\{111\}\langle 110 \rangle$  and  $\{110\}\langle 110 \rangle$  slip systems (b). RD and TD are given as an arbitrary in-plane reference coordinate system. Compression (50% engineering thickness reduction) was conducted along the normal direction ND.



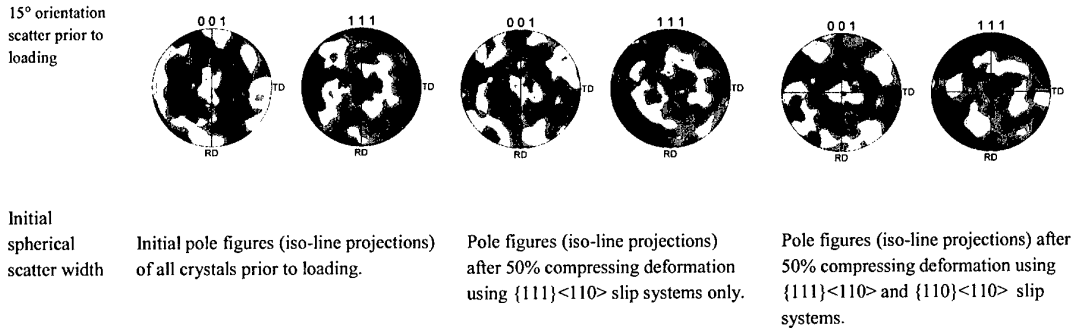
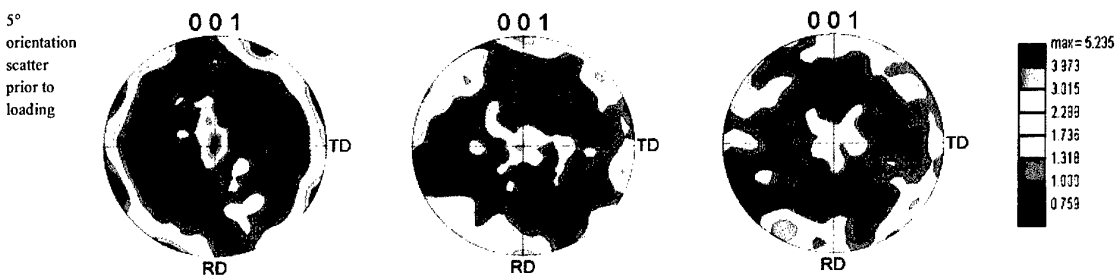


Fig. 8. Effect of the initial orientational scatter width on the in-grain texture evolution presented in terms of iso-line pole figures after deformation with  $\{111\}\langle 110 \rangle$  slip systems (a);  $\{111\}\langle 110 \rangle$  and  $\{110\}\langle 110 \rangle$  slip systems (b). RD and TD are given as an arbitrary in-plane reference coordinate system. Compression (50% engineering thickness reduction) was conducted along the normal direction ND.

A direct comparison of the pole figure data is given in Fig. 9. It documents the tendency of the compressed Cube oriented crystals that the orientational scatter evolving in them increases with the initial orientation spread among neighboring grain portions and with an increasing number of glide systems.



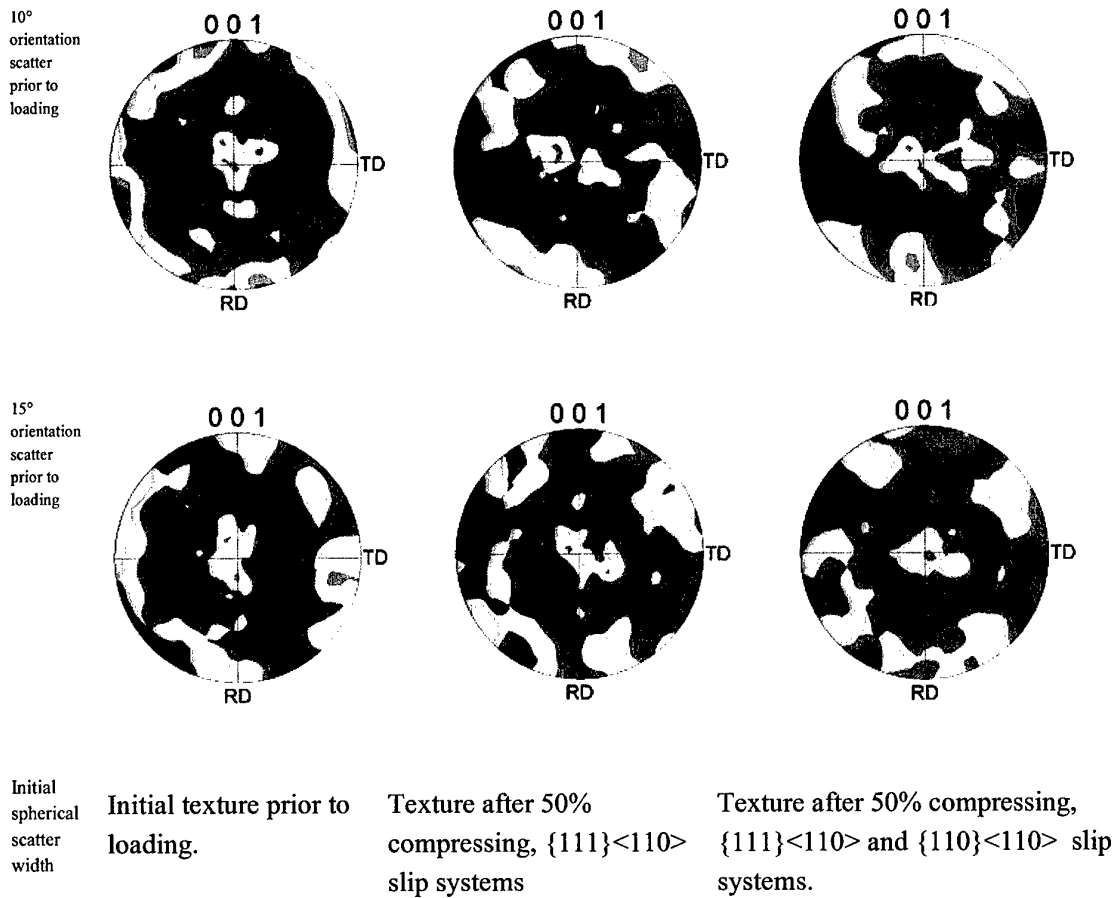
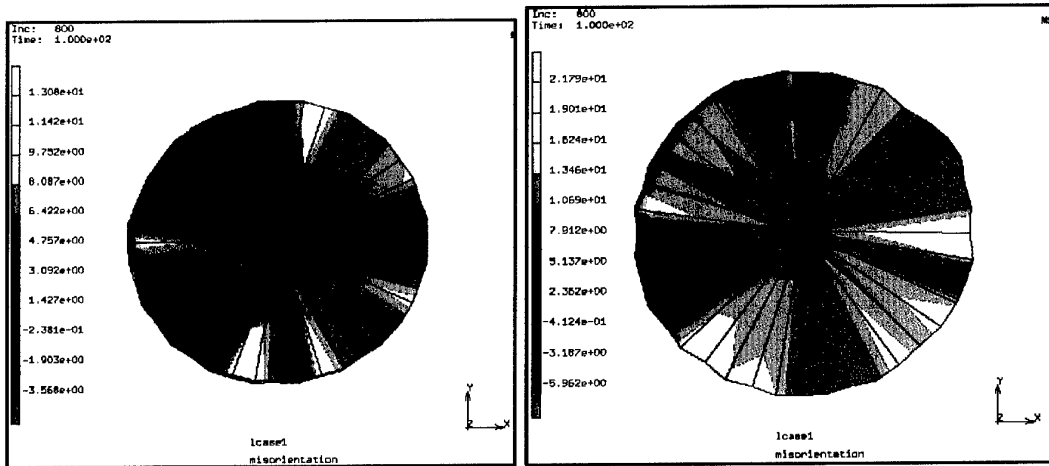


Fig. 9. Direct comparison of data given in Figs. 7 and 8 for {001} pole figures.

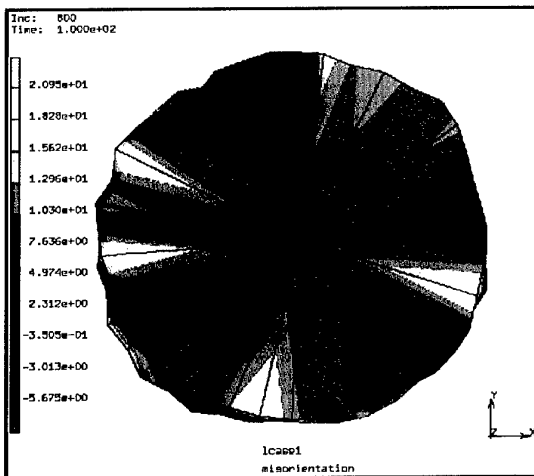
### 6.3 Effect of orientational scatter prior to loading on the lateral misorientation arrangement and on the mechanical properties (<001> axis parallel to compression axis) using {111}<110> slip systems

Figs. 10-12 show the effects of the initial spherical scatter width on the lateral arrangement of the in-grain texture evolution and mechanical properties for close-to-cube oriented grains. The simulations were conducted for {111}<110> slip systems. The data show the misorientation data after 50% compressing deformation.



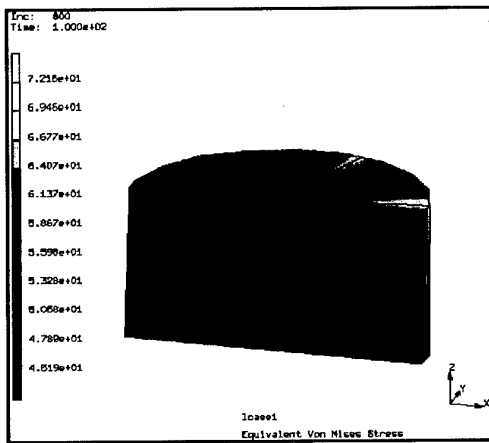
Lateral in-grain misorientation distribution,  
5° orientation scatter prior to loading

Lateral in-grain misorientation distribution,  
10° orientation scatter prior to loading

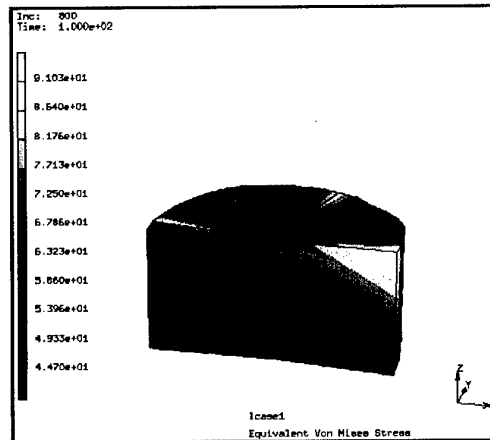


Lateral in-grain misorientation distribution,  
15° orientation scatter prior to loading

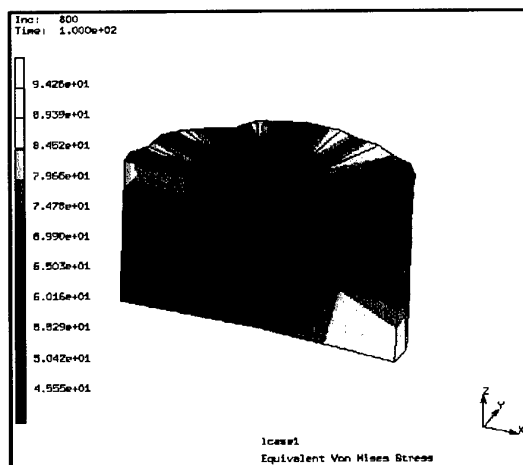
Fig. 10. Influence of the initial orientational scatter (5°, 10°, 15°) on the lateral arrangement of the in-grain texture evolution for close-to-cube oriented grains. The simulations were conducted for  $\{111\}\langle 110 \rangle$  slip systems. The data show the misorientation data after 50% compressing deformation.



Lateral in-grain distribution of von Mises stress, 5° orientation scatter prior to loading



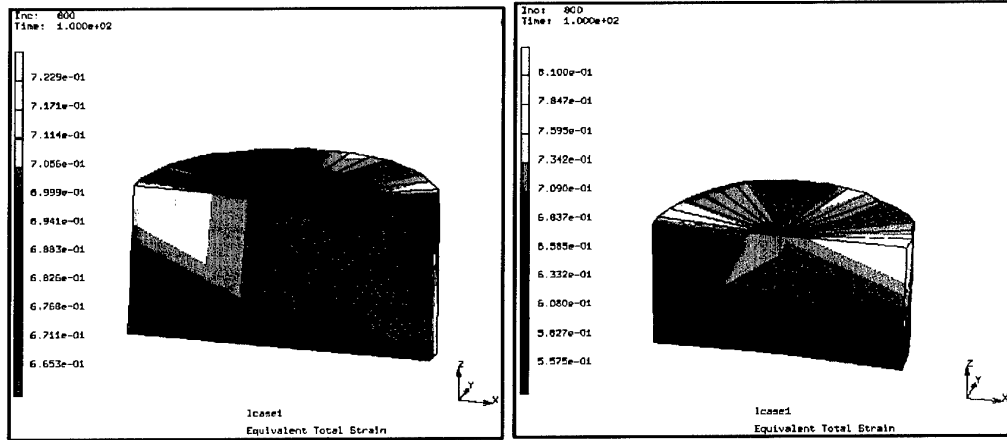
Lateral in-grain distribution of von Mises stress, 10° orientation scatter prior to loading



Lateral in-grain distribution of von Mises stress, 15° orientation scatter prior to loading

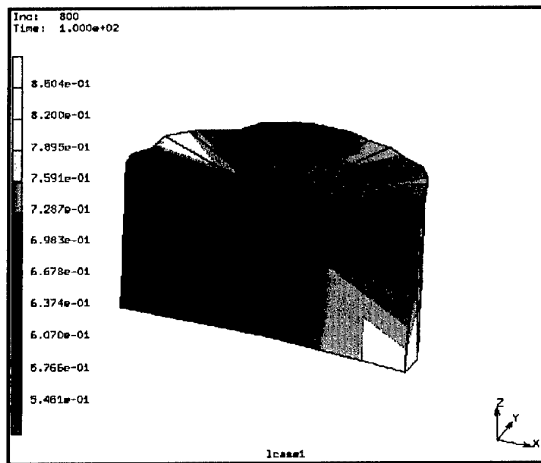
Fig. 11. Influence of the initial orientational scatter (5°, 10°, 15°) on the lateral arrangement of the in-grain von Mises stress for close-to-cube oriented grains. The simulations were conducted for  $\{111\}\langle 110 \rangle$  slip systems. The data show the misorientation data after 50% compressing deformation.





Lateral in-grain distribution of equivalent total strain,  
5° orientation scatter prior to loading

Lateral in-grain distribution of equivalent total strain,  
10° orientation scatter prior to loading



Lateral in-grain distribution of equivalent total strain,  
15° orientation scatter prior to loading

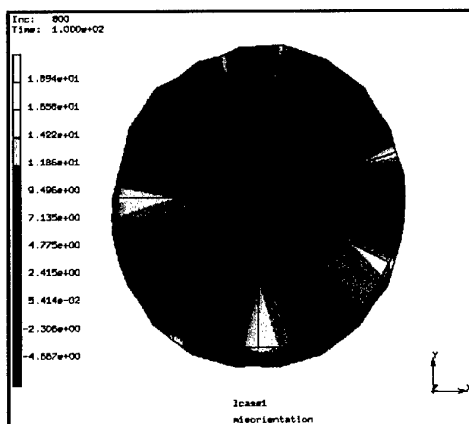
Fig. 12. Influence of the initial orientational scatter (5°, 10°, 15°) on the lateral arrangement of the equivalent in-grain total strain for close-to-cube oriented grains. The simulations were conducted for {111}<110> slip systems. The data show the misorientation data after 50% compressing deformation.



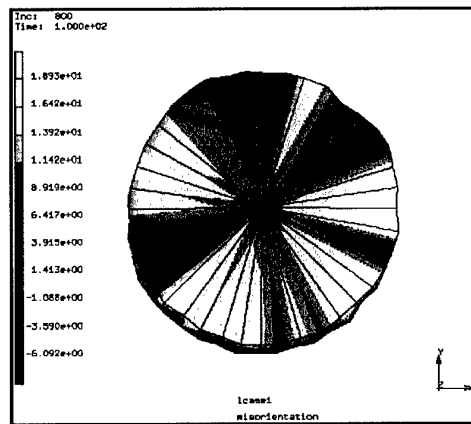


#### 6.4 Effect of orientational scatter prior to loading on the lateral misorientation arrangement and on the mechanical properties ( $\langle 001 \rangle$ axis parallel to compression axis) using $\{111\}[110]$ and $\{110\}[110]$ -type slip systems

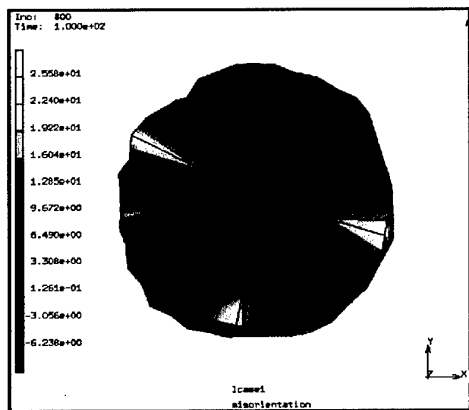
Figs. 13-15 show the effects of the initial spherical scatter width on the lateral arrangement of the in-grain texture evolution and mechanical properties for close-to-cube oriented grains. The simulations were conducted for **octahedral and non-octahedral slip systems**. The data show the misorientations and mechanical properties after 50% compressing deformation.



Lateral in-grain misorientation distribution,  
5° orientation scatter prior to loading



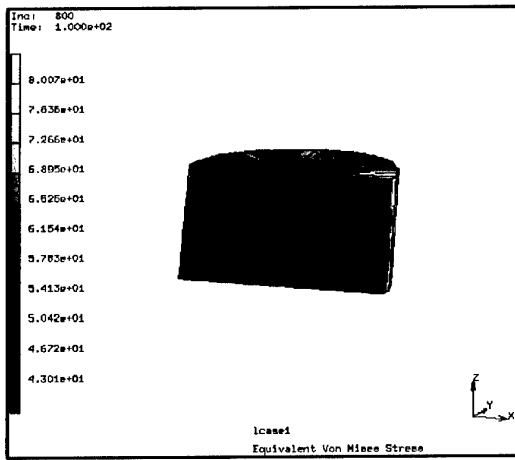
Lateral in-grain misorientation distribution,  
10° orientation scatter prior to loading



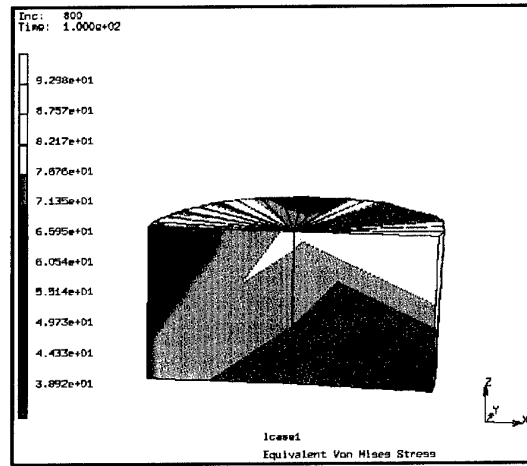
Lateral in-grain misorientation distribution,  
15° orientation scatter prior to loading

Fig. 13. Influence of the initial orientational scatter (5°, 10°, 15°) on the lateral arrangement of the in-grain texture evolution for close-to-cube oriented grains. The simulations were conducted for  $\{111\}[110]$  and  $\{110\}[110]$ -type slip systems. The data show the misorientation data after 50% compressing deformation.

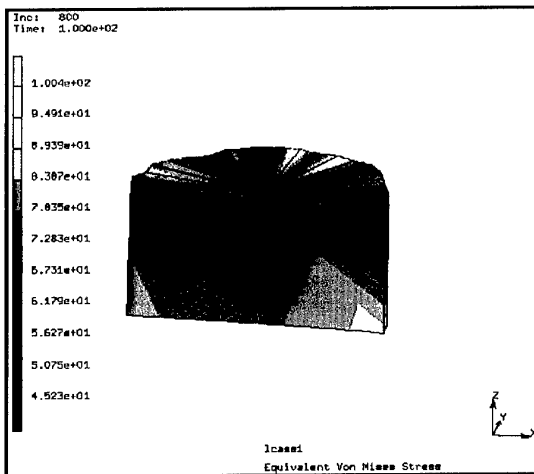




Lateral in-grain distribution of von Mises stress,  
5° orientation scatter prior to loading



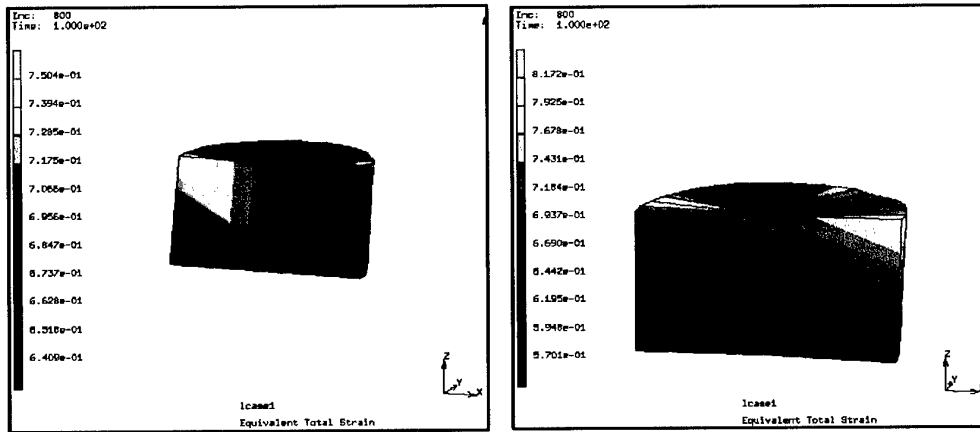
Lateral in-grain distribution of von Mises stress,  
10° orientation scatter prior to loading



Lateral in-grain distribution of von Mises stress,  
15° orientation scatter prior to loading

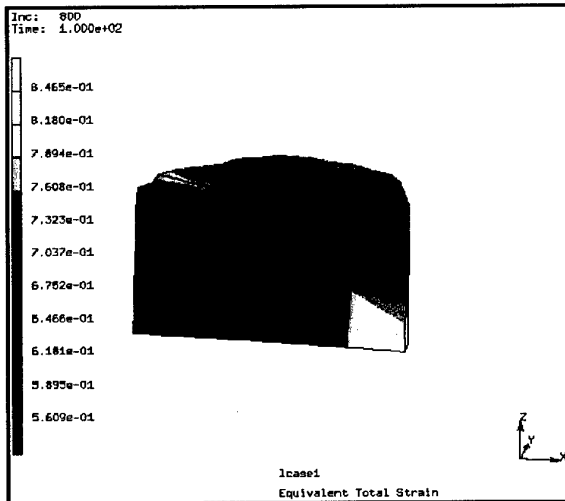
Fig. 14. Influence of the initial orientational scatter (5°, 10°, 15°) on the lateral arrangement of the in-grain von Mises stress for close-to-cube oriented grains. The simulations were conducted for  $\{111\}[1\bar{1}0]$  and  $\{110\}[1\bar{1}0]$ -type slip systems. The data show the misorientation data after 50% compressing deformation.





Lateral in-grain distribution of equivalent total strain, 5° orientation scatter prior to loading

Lateral in-grain distribution of equivalent total strain, 10° orientation scatter prior to loading



Lateral in-grain distribution of equivalent total strain, 15° orientation scatter prior to loading

Fig. 15. Influence of the initial orientational scatter (5°, 10°, 15°) on the lateral arrangement of the equivalent in-grain total strain for close-to-cube oriented grains. The simulations were conducted for {111}[110] and {110}[110]-type slip systems. The data show the misorientation data after 50% compressing deformation.



## 6.5 Influence of friction on in-grain texture evolution and grain fragmentation for a cube-oriented grain

### Introduction

This chapter presents a study on the sensitivity of the simulation of in-grain orientational fragmentation with respect to friction conditions. It is particularly the Cube orientation which in experiments reveals substantial differences in its in-grain texture evolution as a function of the friction conditions. In order to scan various boundary conditions the simulations are conducted using plane strain conditions. The starting texture of the Cube crystals is described in terms of a spherical Gaussian. Orientational in-grain heterogeneity occurring during loading can, therefore, be investigated as a function of friction and orientation scatter.

Fig. 16 shows the assembly of the finite element model. Four surfaces were used to describe the boundary conditions for the simulated plane strain compression tests. This geometry and individual surface treatment was chosen to mimic macroscopic boundary conditions typical of a channel die experiment. The sample consisted of 500 three-dimensional linear elements each with 8 integration points. The simulations used  $\{111\}\langle 110 \rangle$  slip systems. Different friction coefficients (linear Coulomb law) were used to investigate the influence of shear. All simulations were conducted to 50% engineering thickness reduction.

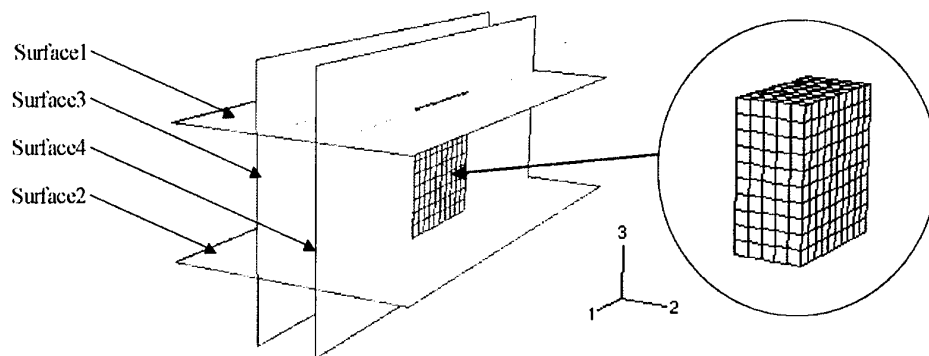


Figure 16 Setup of the finite element model (500 3D linear elements). Four rigid surfaces were used to simulate the boundary conditions during plane strain compression, in particular different friction conditions of the different surfaces.

### Orientalional stability of an ideal cube single crystal

Fig. 17 shows the simulation results obtained for the plane strain compression of an initially *exactly* cube oriented and perfectly homogeneous single crystal, i.e. all elements had the *same* initial orientation  $\varphi_1=0^\circ$ ,  $\phi=0^\circ$ ,  $\varphi_2=0^\circ$  without any initial orientation scatter). The friction coefficients on the top surface (contact surface with compression plane) and bottom surface (surfaces 1 and 2 in Fig. 16) were  $\mu=0.1$ . The friction coefficients on the two side surfaces were zero. Fig. 3 shows that the elements preserved a regular brick-like shape after 50% deformation (engineering strain measure). The gray scale color code describes the von Mises stress. It is very homogeneous throughout the specimen. The  $\{111\}$  pole figure shows that orientational splitting occurred only about ND. The orientation scatter is very symmetric.

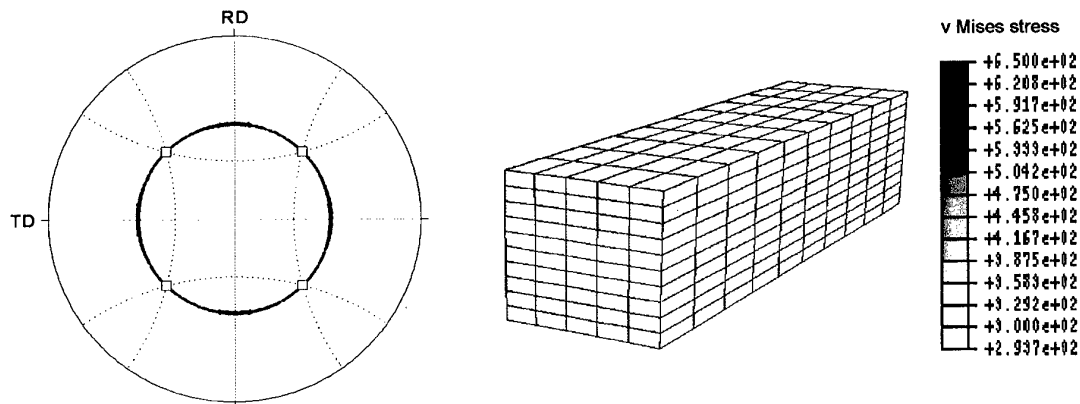


Figure 17 Simulation result for plane strain compression of a cube single crystal. An exact cube orientation ( $\varphi_1=0^\circ$ ,  $\phi=0^\circ$ ,  $\varphi_2=0^\circ$ ) without any initial orientation scatter was assigned to all elements prior to loading. The friction coefficient on surfaces 1 and 2 was  $\mu=0.1$ . The sample was 50% reduced in thickness (engineering strain measure).

### Orientalional stability of a cube single crystal with Gaussian orientation scatter

As-crystallized grains are never perfect but contain lattice defects prior to loading, i.e. the orientation distribution in single grains is neither a delta function in orientation space nor laterally constant. The microtexture in a real single crystal can, therefore, be described in the form of an *ideal* (or *exact*) orientation together with an orientational scatter around it. In the framework of the texture component method introduced above I describe the starting texture of the cube single crystal in the form of a spherical Gauss component with a full width at half maximum of  $2.5^\circ$ . This means that I map a set of single orientations onto the finite element mesh



which satisfies a spherical Gaussian central function about the ideal cube orientation (Fig. 18). The 500 discrete orientations were assigned in random lateral order to the elements of the finite element mesh.

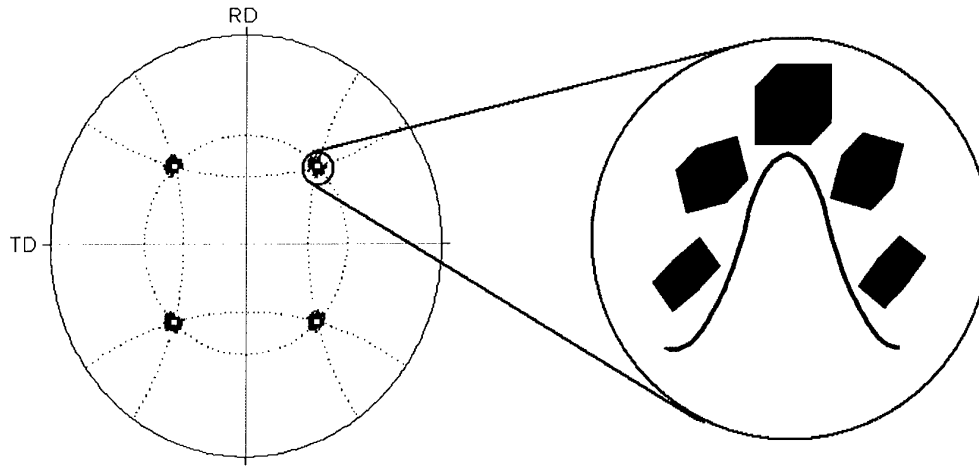


Figure 18 Gauss-type spherical approximation of the initial microtexture within a cube single crystal consisting of 500 single orientations in a stereographic  $\{111\}$  pole figure projection. The full width at half maximum amounts to  $2.5^\circ$ .

Fig. 19 shows the deformation results for this set-up. The other simulation parameters were identical to those used in the previous section. In clear difference to the results for the perfect initial cube orientation which shows that orientation splitting occurs about ND and RD. Fig. 22a shows the corresponding section from the orientation distribution function (ODF). It clearly reveals that the orientation spread after deformation is larger about RD ( $\sim 22^\circ$  for  $f(g)=10$ ) than about ND ( $\sim 14^\circ$  for  $f(g)=10$ ). It must be noted in this context that the data which are exactly located on one of the two axes correspond to pure RD or respectively ND rotations. The finite element mesh and the stress distribution shows that slight shear distortion occurred in most elements.

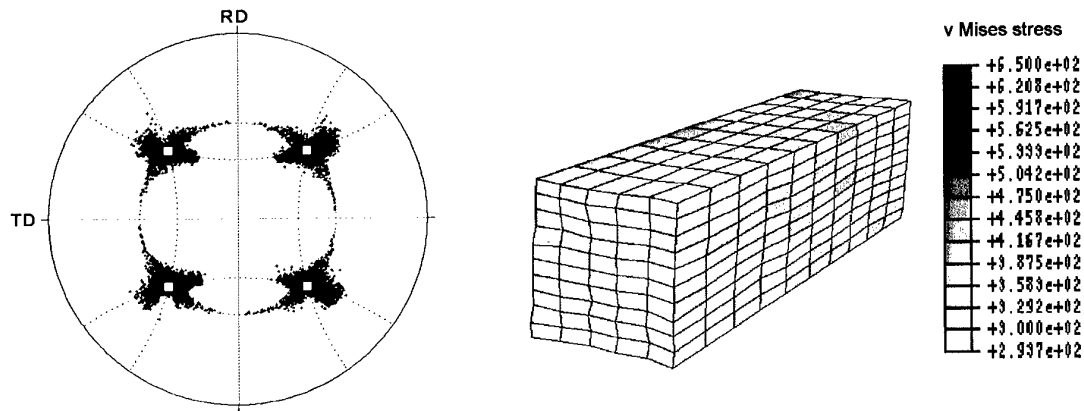


Figure 19 Simulation results for plane strain compression of a single crystal with a  $2.5^\circ$  spherical Gaussian orientation scatter about the exact cube orientation prior to loading. Friction occurs only on surfaces 1 and 2 (top and bottom) with a friction coefficient of  $\mu=0.1$ . See also the ODF section in Fig. 22.

### **Orientational stability of a cube single crystal with Gaussian orientation scatter under large-friction conditions**

Fig. 20 shows the simulation results for the same case as presented in Fig. 19, but the friction coefficient amounted to  $\mu=0.3$ . All other parameters were the same as in Fig. 19. Orientation splitting during forming clearly increases with larger friction on the top and bottom surfaces. Although the re-orientation behavior of most elements is similar to that shown in Fig. 19 additional orientation scatter appears about TD. The scatter about the ND axis (Fig. 22b) is smaller than that for the data shown in Figs. 19 and 22a. It is also important to note that the overall orientational scatter in Fig. 20 is more smeared out than that for the case with smaller friction (Fig. 19). This is also shown by the ODF which reveals a much smaller maximum in the orientation density at the exact cube component (Fig. 22b) when compared to that for the case shown in Fig. 22a. Another difference to Fig. 19 is that Fig. 20 shows more pronounced element distortion and a more inhomogeneous stress distribution.



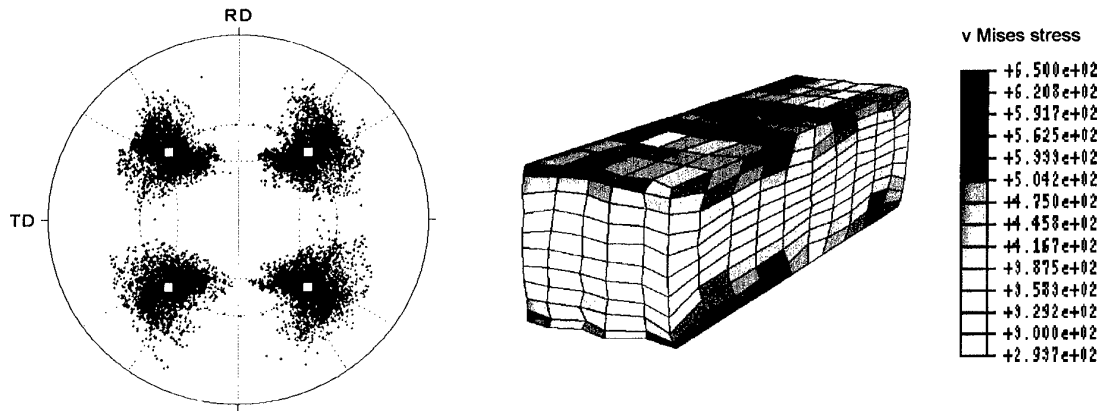


Figure 20 Simulation results for plane strain compression of a single crystal with a  $2.5^\circ$  spherical Gaussian orientation scatter about the exact cube orientation prior to loading. Friction only occurs on surfaces 1 and 2 (top and bottom) with a friction coefficient of  $\mu=0.3$ . See also the ODF section in Fig. 22.

### **Orientational stability of a cube single crystal with Gaussian orientation scatter under surround friction conditions**

Fig. 21 shows the simulation results obtained for plane strain compression of a cube single crystal with an initial Gaussian orientation scatter of  $2.5^\circ$  assuming a friction coefficient of  $\mu=0.1$  on all 4 longitudinal surfaces. The other simulation parameters were the same as in Figs. 19 and 20. The orientational scatter shows a strong component about TD together with some weaker ND and RD scatter (Fig. 22c). Particularly the RD scatter is smaller than that for the simulation with non-zero friction on only two surfaces (Figs. 19, 22a).





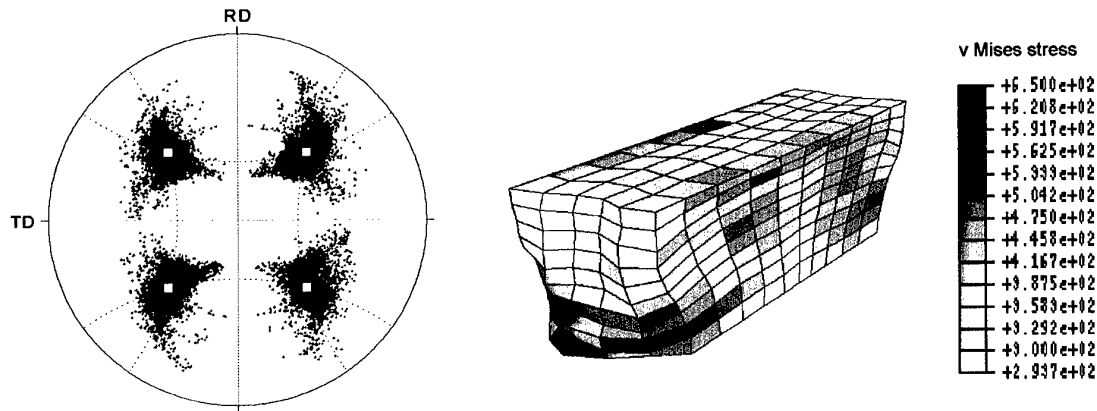


Figure 21 Simulation results for plane strain compression of a single crystal with a  $2.5^\circ$  spherical Gaussian orientation scatter about the exact cube orientation prior to loading. Friction occurs on 4 surfaces with a friction coefficient of  $\mu=0.1$ . See also the ODF section in Fig. 22.

### Influence of initial orientation scatter and of friction on the re-orientation behavior of cube crystals

Comparison of the results for an *ideal* initial cube texture (Fig. 17) and for an initial Gaussian orientation scatter (Figs. 18, 19) for *identical* friction conditions reveals that the simulation method is sufficiently sensitive to account for effects arising from fine changes in starting texture.

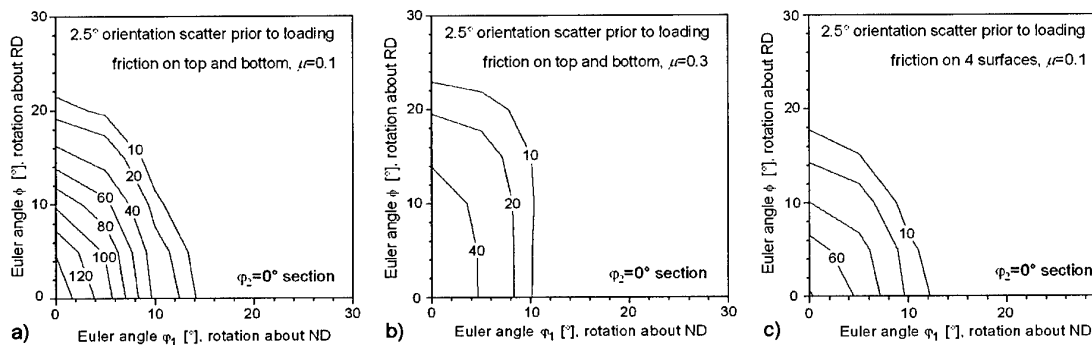


Figure 22 Quantitative presentation of the in-grain orientation spread resulting after deformation in terms of  $\phi_2=0^\circ$  sections from the orientation distribution function (ODF) for the three examples given in Figs. 5-7 in terms of pole figures (ND: normal direction; RD: rolling direction). The data which are exactly located on one of the two axes correspond to pure RD or respectively ND rotations.

- a)  $2.5^\circ$  orientation scatter prior to loading, friction on top and bottom,  $\mu=0.1$
- b)  $2.5^\circ$  orientation scatter prior to loading, friction on top and bottom,  $\mu=0.3$
- c)  $2.5^\circ$  orientation scatter prior to loading, friction on 4 surfaces,  $\mu=0.1$



These results confirm many experiments, namely, that the cube orientation is metastable under plane strain conditions. This was also found in recent theoretical studies on the re-orientation behavior of different orientations by use of homogenization and crystal plasticity finite element analysis [17]. This investigation also confirmed that orientation gradients in initially uniform cube crystals can occur under gradient-free external loads. The intrinsic origin of this effect was quantified in terms of the change in crystal re-orientation upon small changes in initial orientation. Such starting conditions are in the present study represented by the Gaussian orientation scatter prior to deformation. The theory was formulated as a divergence operator applied to re-orientation rate vector fields. The obtained scalar divergence function gave an excellent quantification of the stability of grains under homogeneous boundary conditions as a function of their orientation. Positive divergence which is a source in the re-orientation rate vector field characterize orientations with diverging non-zero reorientation rates which are kinematically unstable and prone to build up orientation gradients. Besides such basic kinematical interpretation I attribute the deviation between Figs. 17 and 19 also in terms of the loss in *local* symmetry (Fig. 19). The slight element distortion shows that due to the laterally random distribution of the imposed initial  $2.5^\circ$  orientation scatter the plane strain state is locally violated entailing strong RD rotations (Fig. 22). These observations correspond to recent results which showed that weakly positive divergent orientations, such as cube in FCC, reveal a larger dependence of their re-orientation behavior on the local mechanical boundary conditions (local deviation from a plane strain state) and, therefore, a larger variety of the resulting orientation spreads, than less divergent crystals. Such effects arising from the loss in local symmetry are surely assisted by friction. However, the influence of friction is likely to promote TD rotations rather than RD rotations because it induces longitudinal shear strains. With increasing friction coefficient and increasing number of surfaces imposing non-zero friction, the orientation and stress distribution becomes increasingly heterogeneous.

### Conclusions for the friction study

This section discussed the orientational stability of Cube FCC crystals under plane strain (50% engineering thickness reduction) by use of a texture component crystal plasticity finite element method (12 slip systems). The main results are:

- If the friction is small ( $\mu=0.1$ ) and the initial orientation of the sample is *exactly* cube everywhere in the mesh (all elements have the *same* initial orientation  $\varphi_1=0^\circ$ ,  $\phi=0^\circ$ ,  $\varphi_2=0^\circ$  without any initial orientation scatter prior to loading) the orientation spread after deformation can be described in terms of a pure ND rotation.
- If the friction is small ( $\mu=0.1$ ) and the initial orientation of the sample is a cube orientation with  $2.5^\circ$  spherical Gaussian scatter the orientation spread after deformation can be described in terms of ND *and* RD rotations.
- If the friction is large ( $\mu=0.3$ ) and the initial orientation of the sample is a cube orientation with  $2.5^\circ$  spherical Gaussian scatter the orientation spread after deformation can be described in terms of ND, RD, *and* TD rotations. The latter rotation mode is due to the induced forward shear.



## 6.6 Improved FE model set-up with finer mesh – simulation of Cube and 90° inclined Cube compression

### Mesh design and FE set-up

The second approach for an improved meshing used again a cylinder with 10 mm in diameter and 15 mm in height. **Different initial crystallographic orientations** parallel to the loading axis were used for the simulations. Compression was conducted at a simulated temperature of 1450 K (1177 °C), The strain rate was varied between  $0.005 \text{ s}^{-1}$  and  $0.1 \text{ s}^{-1}$ . The reduction in height amounted to 50 % corresponding to a true strain of about 0.69. The friction in the two contact planes were assumed to be zero.

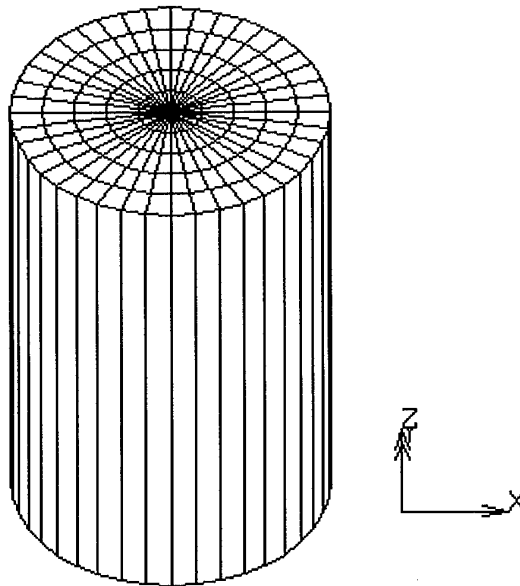


Fig. 23. The improved mesh used for the finite element discretization of the Waspaloy sample. Compression is conducted along the z-axis.

## Constitutive data fit

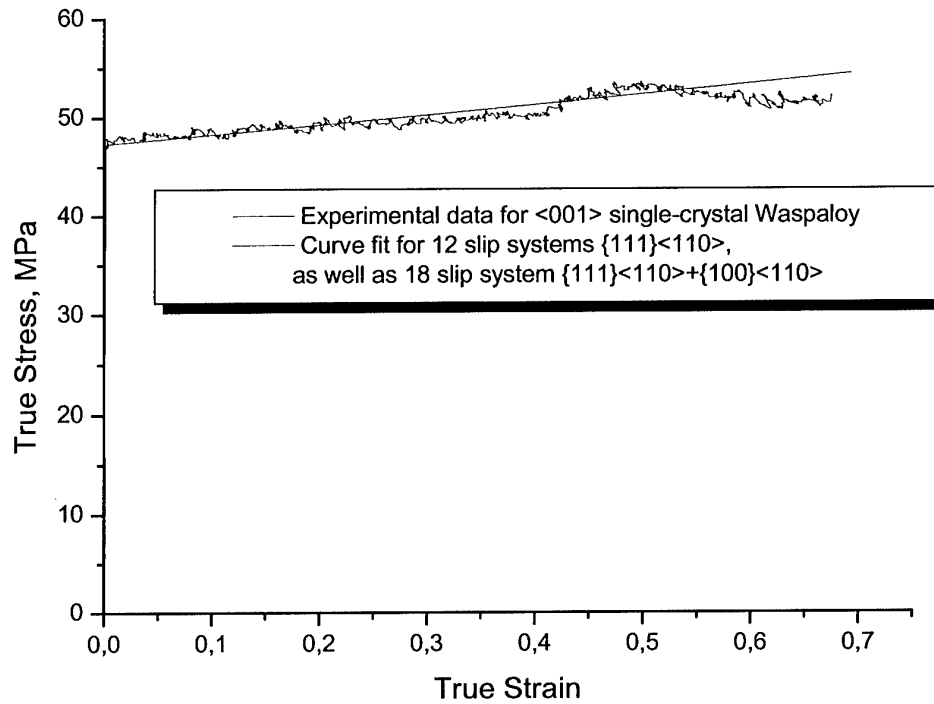


Fig. 24. Constitutive fit for the Cube orientation. Stress-strain response and FEM model fits.

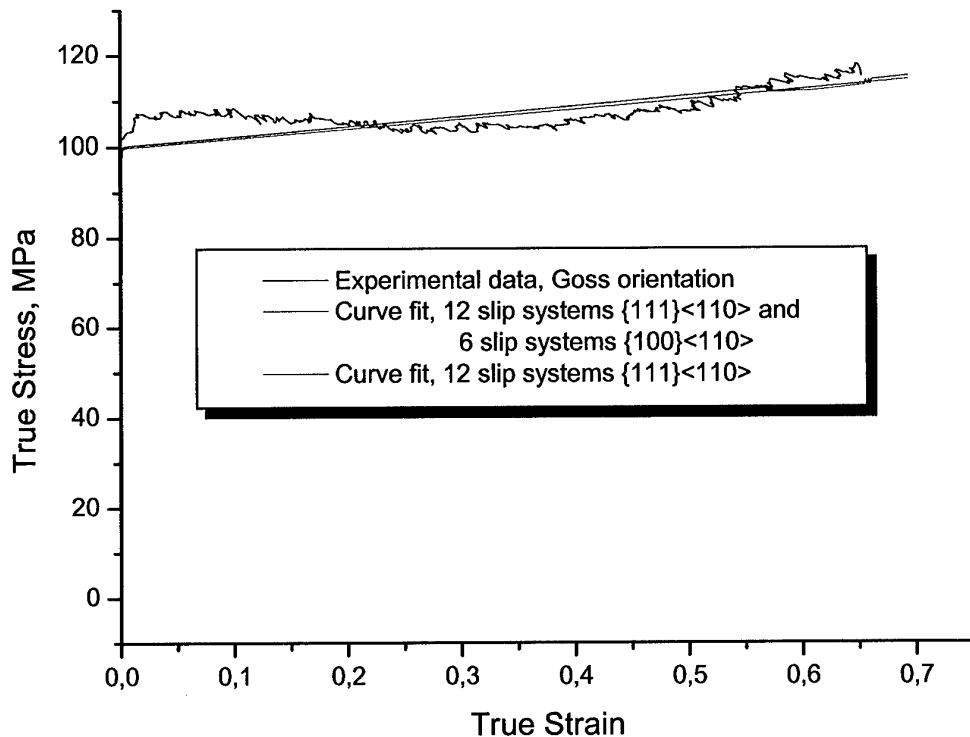


Fig. 25. Constitutive fit for the Goss orientation ( $90^\circ$  TD rotated Cube orientation). Stress-strain response and FEM model fits.

### Texture analysis after compression of a Cube orientation and a Goss orientation

Figs. 26-28 show the pole figures for the Cube and the Goss oriented single-crystal Waspaloy samples after compression deformation. Fig. 4a shows the pole figure results obtained for a crystal plasticity simulation with  $\{111\}\langle 110 \rangle$  slip systems (assumption of low temperature deformation). Fig. 26 shows the pole figures after compression for the Cube orientation. The center of the pole figures corresponds to the compression direction. Fig. 27 reveals the pole figures after compression for the Goss orientation. The simulations were conducted using 12 slip systems  $\{111\}\langle 110 \rangle$ . Fig. 28 shows the corresponding data for the Goss orientation using 18 slip systems  $\{111\}\langle 110 \rangle$  and  $\{100\}\langle 110 \rangle$ . The corresponding microstructures are presented in Figs. 29-31.



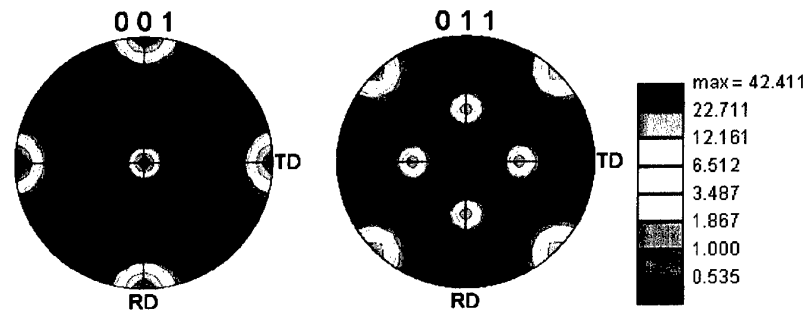


Fig. 26. Pole figures after compression. Center of pole figure corresponds to the compression direction. Cube orientation, same result for 12 slip systems  $\{111\}\langle 110 \rangle$  as well as for 18 slip systems  $\{111\}\langle 110 \rangle$  and  $\{100\}\langle 110 \rangle$ .

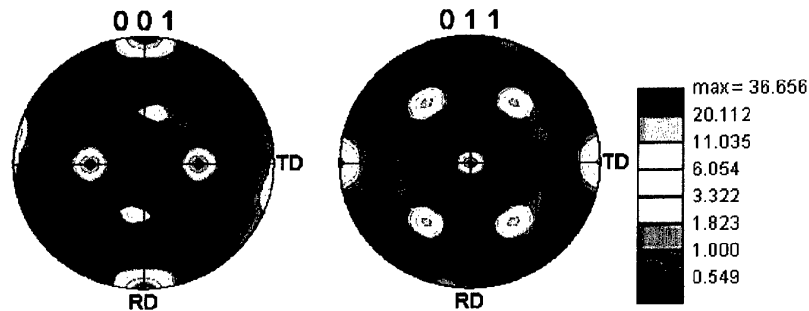


Fig. 27. Pole figures after compression. Center of pole figure corresponds to the compression direction. Goss orientation, 12 slip systems  $\{111\}\langle 110 \rangle$ .

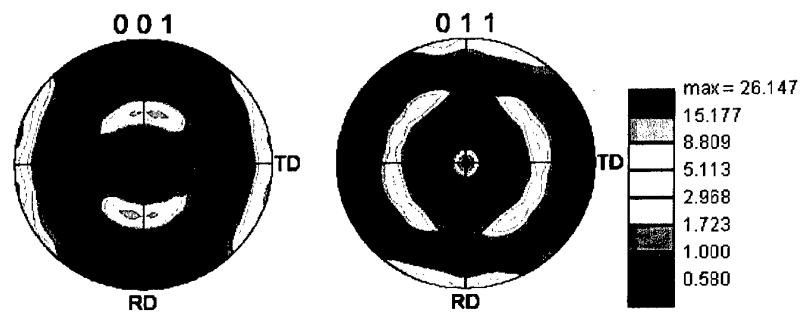


Fig. 28. Pole figures after compression. Center of pole figure corresponds to the compression direction. Goss orientation, 18 slip systems  $\{111\}\langle 110 \rangle$  and  $\{100\}\langle 110 \rangle$ .

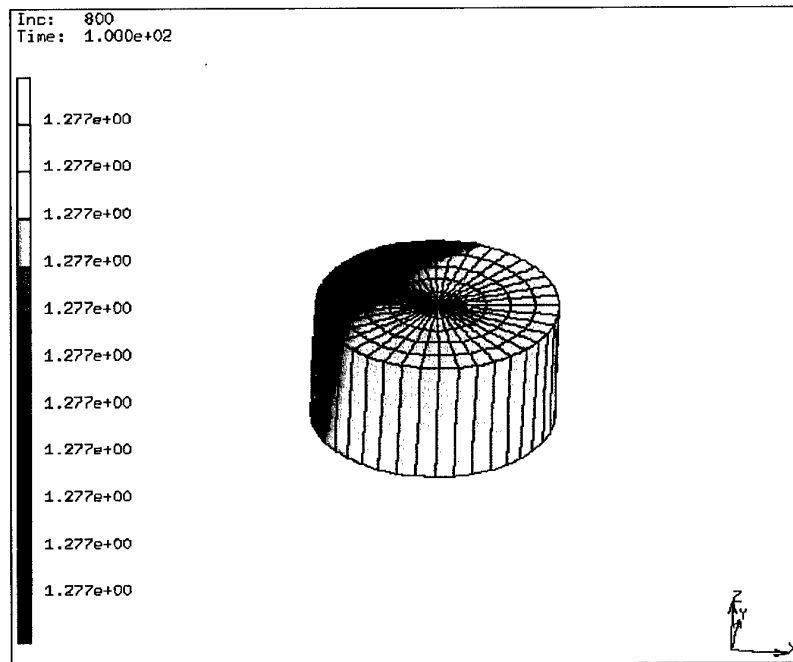


Fig. 29. Lateral in-grain misorientation distribution, Cube orientation, same result for 12 slip systems  $\{111\}\langle 110 \rangle$  as well as for 18 slip systems  $\{111\}\langle 110 \rangle$  and  $\{100\}\langle 110 \rangle$ .

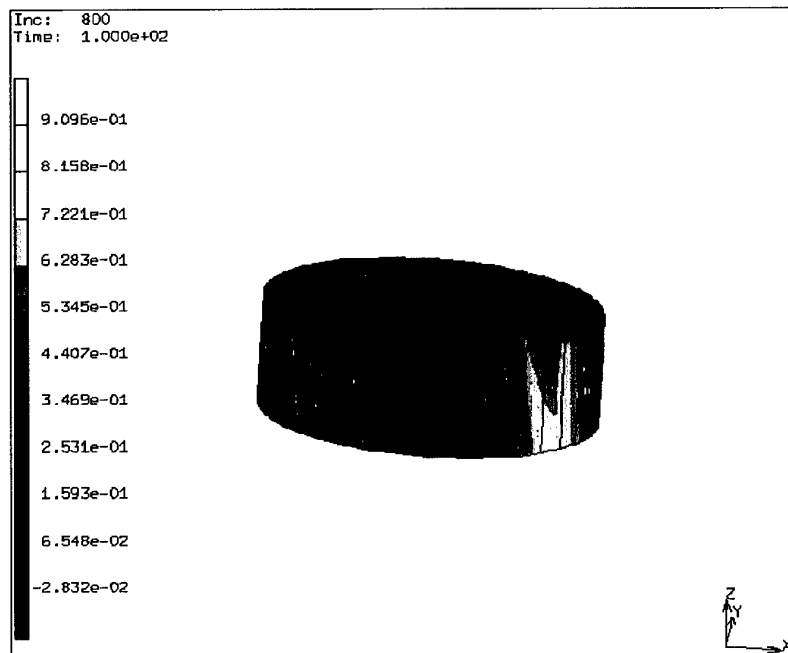


Fig. 30. Lateral in-grain misorientation distribution, Goss orientation, 12 slip systems  $\{111\}\langle 110 \rangle$ .



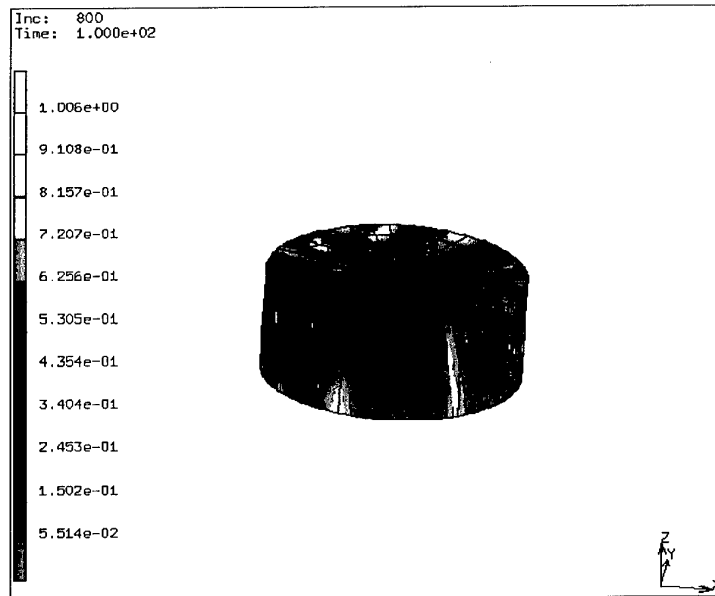


Fig. 31. Lateral in-grain misorientation distribution,  
Goss orientation, 18 slip systems  $\{111\}\langle 110 \rangle$  and  $\{100\}\langle 110 \rangle$ .

## 7. Conclusions

The current study investigated the orientation dependence of the in-grain misorientation development of Waspaloy as a function of the starting orientation. It was found that orientations which are inclined with respect to the Cube orientation reveal a much stronger tendency to undergo orientational grain fragmentation than Cube oriented grains. The Goss orientation reveals a strong tendency towards orientational grain fragmentation when compared to the Cube. Additionally the influence of friction on such phenomena was systematically studied. It was observed that larger friction coefficients lead to a stronger in-grain misorientation development. This aspect is of relevance particularly in cases where Cube oriented as-cast grains cannot be rotated before the deformation.





## References

1. Knowles, D.M., Gunturi, S.: Mater. Sc. Engin. A 328 (2002) 223.
2. Ghosh, R.N, Curtis, R.V., and McLean, M.: Acta metal. Mater. 38(1990) 1977.
3. Österle, W., Bettge, D., Fedelich, B. and Klingelhöffer, H.: Acta mater. 48(2000) 689.
4. Nouailhas, D. and Cailletaud, G.: Scripta Materialia 34(1996) 565.
5. Kalidindi S R, Schoenfeld SE. Mater. Sc. Engin. 2000; A293:120.
6. Arsenlis A, Parks DM. J. Mech. Phys. Solids 2002; 50:1979.
7. Kalidindi SR, Anand L; Metall. Transact. 1993; A24:989.
8. Kalidindi SR, Bronkhorst CA, Anand L. J. Mech. Phys. Solids 1992; 40:537.
9. Raabe D, Klose P, Engl B, Imlau KP, Friedel F, Roters F: Advanced Engineering Materials 4 (2002) 169-180
10. Zhao, Z., Roters, F., Mao, W., Raabe, D.: Adv. Eng. Mater. 3 (2001) 984.
11. Raabe, D., Zhao, Z., Roters, F.: Steel Research 72 (2001) 421.
12. Raabe, D., Roters, F.: International Journal of Plasticity 20 (2004) 339.
13. Raabe, D., Roters, F., Zhao, Z.: Proceedings of the 8th International Conference on Aluminium Alloys in Cambridge, UK, July 2-5, 2002, Materials Science Forum Vols. 396-402 (2002) 31.
14. Raabe, D., Helming, K., Roters, F., Zhao, Z., Hirsch, J.: Proceedings of the 13th International Conference on Textures of Materials ICOTOM 13, 2002, Seoul, Korea, Trans Tech Publications, ed.: Dong Nyung Lee, Materials Science Forum, Vols. 408-412 (2002) 257.
15. MSC. Marc user's manual, Vol.D, MSC Software Corporation, 2001.
16. Hosford, WF, The mechanics of crystals and textured polycrystals, Oxford University Press, Oxford 1993.
17. Raabe D, Z. Zhao, S.-J. Park, F. Roters: Acta Materialia 50 (2002) 421.

